MARK I CONTAINMENT PROGRAM
VENT SYSTEM COMPRESSIBILITY -
EFFECTS ON MARK I POOL SWELL
TASK 9.1.4.3

Prepared for

General Electric Company

by

Acurex

Approved: *[signature]*
P. W. Ianni, Manager
Containment Design

Approved: *[signature]* E. Collins, acting for
G. E. Wade, Manager
Mark I Containment and
SRV Programs

NUCLEAR ENGINEERING DIVISION • GENERAL ELECTRIC COMPANY
SAN JOSE, CALIFORNIA 95125

GENERAL ⒼⒺ ELECTRIC

8011040232

DISCLAIMER OF RESPONSIBILITY

TABLE OF CONTENTS

LIST OF ILLUSTRATIONS

LIST OF ILLUSTRATIONS (Concluded)

NOMENCLATURE/KEYWORDS

Symbols used in the body of this report are defined below.
Figure P-1 shows a typical Mark I wetwell arrangement and illustrates the
components and parameters important to the discussions in this report.

A = flow area, ft^2

A_e = effective pool surface area, ft^2

C_p = specific heat at constant pressure, Btu/lbm ^oF

C_v = specific heat at constant volume, Btu/lbm ^oF

D = downcomer diameter

F = torus load, lbf

$\frac{1}{D}$ = friction and form flow resistance coefficient (dimensionless)

g = gravitational acceleration, ft/sec^2

g_c = gravitational constant = 32.2 $lbm\text{-}ft/lbf\text{-}sec^2$

h = enthalpy, Btu/lbm

h_s = downcomer submergence, ft

$\dot{m}_B$ = mass flowrate into bubble, lbm/sec

P_B = bubble pressure, lbf/ft^2

P_D = initial drywell pressure

P_{fs} = freespace pressure, lbf/ft^2

P_w = initial wetwell pressure

$\dot{P}$ = rate of change of pressure, psi/sec

q = heat loss rate, Btu/sec ft^3

R = specific gas constant

s = entropy, Btu/lbm-^{0}R

SF = scale factor, $\frac{\text{subscale dimension}}{\text{full scale dimension}}$ (dimensionless)

t = time, seconds

T, T_o = stagnation temperature, ^{0}R

T_B = bubble temperature, ^{0}R

T_D = drywell gas absolute temperature

T_i = initial vent temperature, ^{0}F

V, U, v = flow velocity, ft/sec

V_B = bubble volume, ft^3

$\dot{V}_B$ = first time derivative of V_B, ft^3/sec

$\ddot{V}_B$ = second time derivative of V_B, ft^3/sec^2

V_{fs} = freespace volume, ft^3

x = displacement in the direction of flow, ft

ρ = density, lbm/ft^3

η = bubble rise velocity, ft/sec

ϕ = bubble impedance factor, ft

γ = C_p/C_v
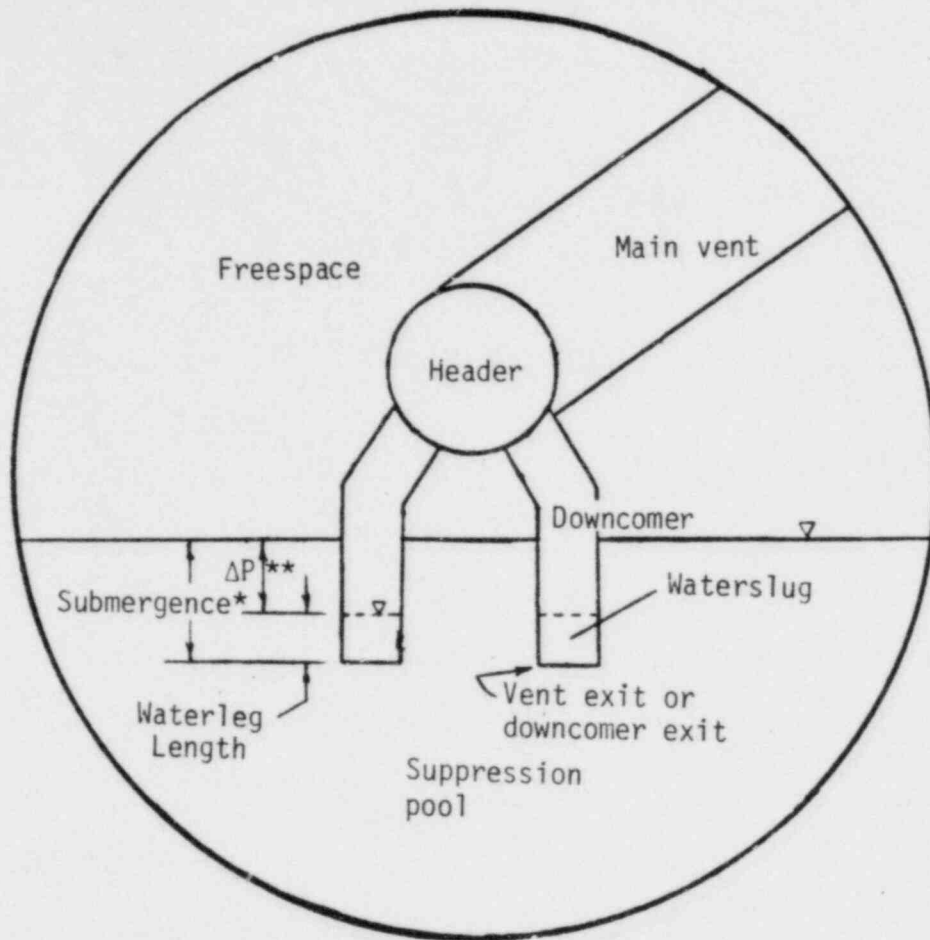
Figure P-1. Mark I wetwell.

*Submergence, given in psi or ft. of water
**ΔP, given in psi or ft. of water or fraction of submergence

SECTION 1

INTRODUCTION

The Mark I Loss-of-Coolant-Accident (LOCA) load definition uses subscale test data to define torus vertical loads during a pool swell transient. Peak download and upload values are derived from Quarter Scale Test Facility (QSTF) plant unique test data. Data from the 3-dimensional EPRI 1/11.7 scale tests provided a circumferential load distribution function used with the QSTF data to establish the complete load definition (Reference 9).

To date, subscale pool swell testing conducted for the Mark I Program has been based on scaling relationships developed by Moody (Section 3). The tests were conducted at ambient temperature, using additional flow resistances in the vent system so that enthalpy flow into the pool was correctly modeled. Flow resistance corrections were based on incompressible flow through the vent/downcomer system. Recent work by Chambré under contract to EPRI (Reference 2) has shown that gas compressibility effects were not correctly modeled in the subscale tests, and comparison between test data and fully compressible model predictions revealed differences in the pressure histories that could potentially affect design loads.

To gain a better understanding of compressibility effects, a computer model was developed which simulates Mark I vent clearing and pool

swell phenomena. The model combines a compressible vent flow model with a pool hydrodynamics model. The vent model was verified independently by demonstrating that it accurately handles various test cases with known solutions. The pool hydrodynamics model was calibrated using QSTF pool swell data. Since applicability of Moody scaling relationships to pool swell hydrodynamics has been repeatedly demonstrated in subscale facilities (Refer nces 5 through 8), the combined vent-clearing/pool-swell model can confidently be used in conjunction with scaling laws to predict the sensitivity of full scale pool swell loads to vent system compressibility effects.

This report briefly discusses Mark I pool swell scaling, describes the newly developed vent-flow/pool-swell model including various test cases, and presents analytical predictions of the effects of vent system compressibility on Mark I pool swell loads.

SECTION 2

SUMMARY OF COMPRESSIBILITY ASSESSMENT

The study reported herein has led to better understanding and successful modeling of vent system compressibility effects. Although compressibility effects were not modeled in previous subscale tests, the tests have been shown to be conservative for existing Mark I conditions. Compressibility effect on peak download ranges from a load increase of 11 percent near full ΔP to a 16 percent decrease at moderate ΔP. Peak upload is uniformly mitigated by compressible effects, typically by about 15 percent. The change in download impulse due to compressibility effects ranges from negligible at full ΔP to a decrease of about 3 percent at small to moderate ΔP.

Additionally, as a part of this study, known differences between actual QSTF test conditions and ideal test conditions have been quantified separately from compressibility effects. Test conservatisms were found to provide 4 to 6 percent added margin in QSTF loads for the case examined.

Compressibility effects in the Mark I vent system are primarily manifestations of vent system acoustic delays which are of the same order as characteristic times of the pool swell transient. Prior to vent clearing, acoustic response to the drywell pressurization ramp causes the downcomer exit pressure and pressure rate to oscillate about the instantaneous drywell values. Following vent clearing, acoustic delays

2-2

retard the development of quasi-steady flow into the bubble, resulting in a mass flow decrement (relative to incompressible flow) which acts to mitigate pool swell response.

SECTION 3

BACKGROUND

Pool swell testing has been conducted in a variety of subscale Mark I facilities (References 1, 5, 6, 7, 8) to better understand post-LOCA response in the Mark I configuration and to confirm analytically derived scaling laws. Typically, a test facility consists of one or more downcomer pairs and their associated vent header and main vent sections mounted in a torus segment so that, based on symmetry arguments the test assembly represents one or more "cells" of a full Mark I contai...ent. All components are geometrically scaled; relative sizes of vents, headers, and so on, are consistent with full scale. During the tests, initial properties (e.g., drywell and wetwell pressure) and instantaneous parameters (e.g., drywell pressurization rate or vent flowrate) are controlled according to scaling considerations to assure pool swell transient performance results which can be scaled up to predict full scale performance.

The Quarter Scale Test Facility (QSTF) consists of a downcomer pair mounted in a torus segment nominally of 1/4 linear scale (actual Mk I torus sizes vary slightly). Vent header/downcomer configuration and cell width (length of the torus segment) can be varied to perform plant unique tests. Drywell pressurization and pool swell is driven by a pressurized air tank which blows down through a burst disk arrangement into the

drywell. Load cells and pressure transducers are used to measure torus loads during pool swell. The QSTF is described in detail in Reference 1.

3.1 POOL SWELL SCALING

References 3 and 4 explain scaling relationships for subscale pool swell tests. From Reference 4, if the following groups are invarient from model to prototype (model is geometric scale of prototype)

$$\pi_1 = \gamma \tag{3-1}$$

$$\pi_2 = \frac{P_w}{\rho g D} \tag{3-2}$$

$$\pi_3 = \frac{P_D}{P_w} \quad \text{(at corresponding values of } t^* = t\sqrt{g/D}) \tag{3-3}$$

$$\pi_4 = C_m \left(\frac{RT_D}{gD}\right)^{1/2} \quad \begin{array}{l}\text{(for all values of dimensionless pressure}\\ \text{drop } (P_D - P)/P_D)\end{array} \tag{3-4}$$

then $(P-P_w)/P_w$ and v/v_0 at a given location will be the same in the model and prototype at the same value of nondimensional time $t^* = t\sqrt{g/D}$. If exact geometric scaling is used in the vent system, $C_{m(model)} \cong C_{m(prototype)}$ (neglecting Re effects) and thus $RT_D \sim D$ which requires either a very heavy gas or low temperature or both. Preserving π_4 by low temperature or heavy gas was not feasible and thus for the QSTF and other subscale tests, the temperature and composition of the gas (air) was not varied and the vent resistance was increased according to $C_m \sim D^{1/2}$ (or $FL/D \sim D^{-1}$). Application of the above approach leads to the relationships in Table 3-1.

TABLE 3-1. SCALING RELATIONSHIPS

Length	$\propto$	scale factor (SF)
Time	$\propto$	$SF^{1/2}$
Pressure	$\propto$	SF
Temperature	$\propto$	SF
Velocity	$\propto$	$SF^{1/2}$
Enthalpy flow $= \rho A V c_p T_o$	$\propto$	$SF^{7/2}$
Mass flowrate $= \rho U A$	$\propto$	$SF^{7/2}$

Two important consequences of resistance scaling should be noted.
First, resistance scaled tests are typically run with geometric similarity
of the vent/downcomer system with one or more orifices inserted to bring
the total system resistance up to the desired value. With lumped flow
resistance, the subscale model does not have the same flow resistance
distribution (also referred to as vent capacitance) as the prototype.
However, judicious placement of the added flow resistances results in a
satisfactory simulation of the full scale flow resistance distribution
(Reference 4). The second consequence of resistance scaling is the
primary focus of this report: vent Mach number varies from model to
prototype. Since temperature is not scaled, sound speed in subscale is
the same as in full scale, but all velocities should go as: length/time ~ SF.

Therefore, in subscale tests, vent system acoustic response has
been too fast. Since the duration of a full scale Mark 1 pool swell
transient has the same order of magnitude as acoustic travel times in the
vent system, acoustic delays will influence full scale pool swell
response. In subscale tests conducted at ambient temperature, acoustic

response can be very short relative to the pool swell transient so the effects of vent system compressibility are less pronounced.

3.2   EPRI/CHAMBRÉ MODEL

Consequences of the failure to preserve Mach number in the vent system were first studied by Prof. Chambré of the University of California at Berkeley under sponsorship of EPRI. Chambré developed a compressible flow model of the vent system in the EPRI 1/11.7 scale facility at Stanford Research Institute (SRI). The vent model solved the compressible flow equations with friction by finite difference methods in the main vent, branch to the vent header and branches into three downcomers. The energy equation was handled by using an experimentally adjusted process exponent. The downcomer flow was coupled to a bubble model based on an analytic solution of a spherical bubble in a semi-infinite pool at a specified depth below the surface. The objective of Chambré's model was to study the mass flow split among the three downcomer pairs that comprise repeating symmetrical sections of a typical Mark I vent system. The model included a simulation of the bubble primarily to provide an appropriate boundary condition for the vent flow calculations.

Results from the model were compared to test results from the 1/11.7 scale tests and found to be in reasonable agreement. Chambré then used the model to predict full scale results by lowering the temperature of the gas and removing the flow restricting orifices. The resulting downcomer exit pressure (Figure 5-9), showed an acoustic delay (compared to drywell pressure) followed by a ramp whose slope exceeded the drywell slope. These results were found to be in agreement with simple pipe acoustic response theory as shown in Section 4.

Chambré's work was not intended to be used to predict containment loads and thus the current study was undertaken to estimate the influence of vent compressibility on containment loads.

3.3   GE/ACUREX MODEL

The GE/Acurex model consists of a fully compressible one-dimensional vent flow model coupled to a semi-empirical bubble/pool-swell model. The vent model solves mass, momentum and entropy equations using a fully implicit technique. It is flexible enough to handle various vent system configurations, using a series of nodes connected by flow paths which can be used to simulate friction loss and area change effects. The flowpath from the drywell to a single downcomer exit is modeled using vent and header flow areas which have been reduced to simulate the effective vent and header areas which service a single downcomer (vent and header flow velocities are preserved). Strictly speaking, a one-dimensional vent flow model cannot simulate acoustic response in a vent system with headers and branches, however, EPRI/Chambré studies (Reference 2) showed that a three-dimensional vent system locks into a single response frequency which corresponds to an "average" vent system length. (Like using the middle pair of downcomers in a one-dimensional model).

At the inlet node (drywell), allowable boundary conditions are: specified flow velocity, specified mass flowrate, or specified pressure with either stagnation temperature or entropy. The user selects isothermal or adiabatic flow within the vent system. At the exit-node (downcomer exit) a pressure-time history may be specified or a bubble model may be selected, in which case the bubble conservation and dynamic growth equations are coupled with the vent exit node conservation equations. The vent model conservation equations and solution scheme are discussed in detail in Section 4.

Development of the bubble model required attention to the basic physics involved in order to accurately simulate bubble and freespace pressure transients as well as the net torus loads. The model uses a modified Rayleigh bubble formulation with an empirically determined impedance factor to simulate the effects of side walls and adjacent bubbles in prototypical bubble growth. Isothermal and adiabatic bubble energy equations are available as options. Bubble dynamics and conservation equations are described in detail in Section 4.

To calculate the final boundary conditions, the instantaneous freespace volume plus the bubble volume is set equal to the initial freespace volume, and freespace pressure is calculated using an empirically determined process exponent.

Since loads ultimately control design decisions, it is advantageous to relate instantaneous wetwell conditions directly to torus loads. The GE/Acurex model calculates vertical loaas during pool swell based on the instantaneous pressure differential between the bubble and the wetwell freespace (minus the effective hydrostatic head of the rising waterslug) and an effective area of application determined from QSTF results.

SECTION 4

GE/ACUREX MODEL

This section provides a detailed description of the GE/Acurex vent-flow/pool-swell model, including development of the finite difference equations solved in the model and the results of various test cases and sensitivity studies.

4.1   VENT MODEL -- GOVERNING EQUATIONS

The basic equations of motion which control events in a one-dimensional vent system are continuity, momentum and energy. These are respectively:

$$\frac{A}{\partial t}\frac{\partial \rho}{} + \frac{\partial \rho u A}{\partial x} = 0 \tag{4-1}$$

$$\rho \frac{\partial u}{\partial t} + \rho u \frac{\partial u}{\partial x} = -\frac{\rho u^2}{2}\frac{4f}{D} - \frac{\partial p}{\partial x} \tag{4-2}$$

$$\rho \frac{\partial (h + u^2/2)}{\partial t} + \rho u \frac{\partial (h + u^2/2)}{\partial x} = q + \frac{\partial p}{\partial t} \tag{4-3}$$

By subtracting u times the momentum equation from the energy equation and introducing the Gibb's relation,

$$dh = Tds + dp/\rho \tag{4-4}$$

an entropy conservation equation is developed, namely

$$\frac{\partial s}{\partial t} + u \frac{\partial s}{\partial x} = \frac{q}{\rho T} + \frac{u^3}{2T} \frac{4f}{D} \qquad (4\text{-}5)$$

The equation set to be solved will include equations (4-1), (4-2), and
(4-5). The choice of the entropy equation, although arbitrary, yields
somewhat simple algebra and the ability to deal with a primary variable
that is nearly invariant in many practical situations.

The nodal grid selected for treatment is shown in Figure 4-1. It
is presumed that the primary variables change linearly between adjacent
grid positions. Time derivatives are represented with a linear backward
difference of the form

$$\frac{dy}{dt}\bigg|_t = \frac{y_t - y_{(t - \Delta t)}}{\Delta t} \qquad (4\text{-}6)$$

where y is any variable. This formulation will assure a valid steady
state solution set when Δt becomes very large.

Use of backward difference techniques also avoids the problems
introduced by "stiff" equation sets which may be locally introduced in the
overall nodal representation.

Introducing relations of the form of equation (4-6) into equation
(4-1), (4-2), and (4-5) yields the following set of ordinary differential
equations

$$A\,(\rho - \rho^0) + \Delta t\,\frac{d(\rho u A)}{dx} = 0 \qquad (4\text{-}7)$$
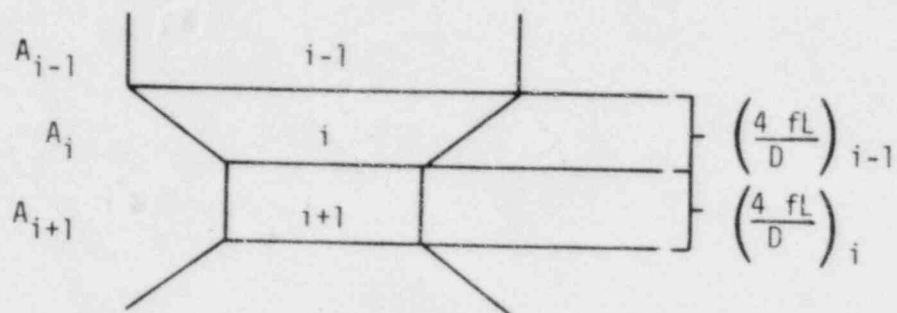
Figure 4-1. Nodal System.

$$(u-u^0)/\Delta t + u \frac{du}{dx} = \frac{-u|u|}{2} \frac{4f}{D} - \frac{1}{\rho} \frac{dp}{dx} \qquad (4-8)$$

$$(s-s^0)/\Delta t + u \frac{ds}{dx} = \frac{q}{\rho t} + \frac{|u^3|}{2T} \frac{4f}{D} \qquad (4-9)$$

where p^0, u^0, s^0 refer to values of the variables at the previous time increment.

To reduce these equations to algebraic relations, each is integrated between successive nodal points. Assuming that $1/\rho$, u, ρA, p, s, $u|u|f/D$, $q/\rho t$, and $|u^3|f/DT$ each vary linearly between nodes, integration of Equations 4-7, 4-8 and 4-9, yields:

$$(\rho_i - \rho^0_i) A_i + (\rho_{i-1} - \rho^0_{i-1}) A_{i-1}$$
$$+ 2\Delta t(\rho_i u_i A_i - \rho_{i-1} u_{i-1} A_{i-1})/\Delta x = 0 \qquad (4-10)$$

$$(u_i + u_{i-1} - u^0_i - u^0_{i-1})/\Delta t + (u_i^2 - u_{i-1}^2)/\Delta x$$

$$= -2 (u_i|u_i| + u_{i-1}|u_{i-1}|)\left(\overline{\frac{f}{D}}\right) - (\frac{1}{\rho_i} + \frac{1}{\rho_{i-1}}) \frac{P_i - P_{i-1}}{\Delta x} \qquad (4\text{-}11)$$

$$(s_i + s_{i-1} - s^0_i - s^0_{i-1})/\Delta t + (u_i + u_{i-1})(s_i - s_{i-1})/\Delta x$$

$$= 2 \left(\overline{\frac{q}{\rho T}}\right) + 2 \left(\left|\frac{u_i^3}{T_i}\right| + \left|\frac{u_{i-1}^3}{T_{i-1}}\right|\right) \left(\overline{\frac{f}{D}}\right) \qquad (4\text{-}12)$$

These equations represent a series of 3N-3 simultaneous nonlinear algebraic equations with 3N primary unknown quantities. Specifically these primary unknowns are taken to be density, velocity and entropy. Temperature and pressure are obtained from the state relations.

$$\ln(T/T^0) = (s-s^0)/C_v + (\gamma - 1)\ln(\rho/\rho^0) \qquad (4\text{-}13)$$

$$p = \rho RT/m \qquad (4\text{-}14)$$

Three boundary conditions are required to close this set of equations. One is provided at the initial node through specification of mass flow rate, velocity or pressure histories. A second is also provided at the initial node by specifying values of entropy or total enthalpy. The final boundary condition is imposed either explicitly or implicitly at the last node and relates to the bubble dynamics. An explicit formulation can specify a pressure time history within the bubble. Implicit representation involves additional relations for bubble dynamics which couple with conditions at the vent exit.

4.2   VENT MODEL -- TEST CASES

1.   Isentropic Nozzle Flow -- The vent flow model was run with mass
      flowrate fixed at the inlet and pressure fixed at the exit.
      There was a single area change in the vent system and no
      friction losses. The model quickly settled on a steady state
      solution, and the resulting values of pressure, temperature,
      velocity, etc., agreed with isentropic flow table values.

2.   Constant Area Fanno Flow -- The vent flow model was again run
      with mass flowrate fixed at the inlet and pressure fixed at the
      exit. Flow area was constant throughout the vent system, and
      friction losses were specified between nodes. Steady state
      values of pressure, temperature, etc., calculated by the
      program were found to agree with Fanno flow table values.

3.   Transient Ramp Pressure at Entrance to Dead-end Pipe -- This
      test case was run to check the model against the small
      perturbation theory result of Reference 5. The vent model was
      run 'backward', with a specified mass flowrate of zero lbm/sec
      at the vent entrance to simulate a closed end and a ramped
      pressure (0.1 psi/sec) specified at the vent exit. The vent
      was a straight pipe, 50 ft long, with no friction losses.
      Program and theoretical results show excellent agreement
      (Figure 4-2).

4.   Timestep Sensitivity -- Test Case 3 was repeated at timestep
      sizes ranging from 0.0005 to 0.008 seconds (Figure 4-3). With
      larger timesteps, the program converges more quickly on a
      steady-state solution. As timestep size is reduced, the
      program solution approaches the theoretical solution shown in
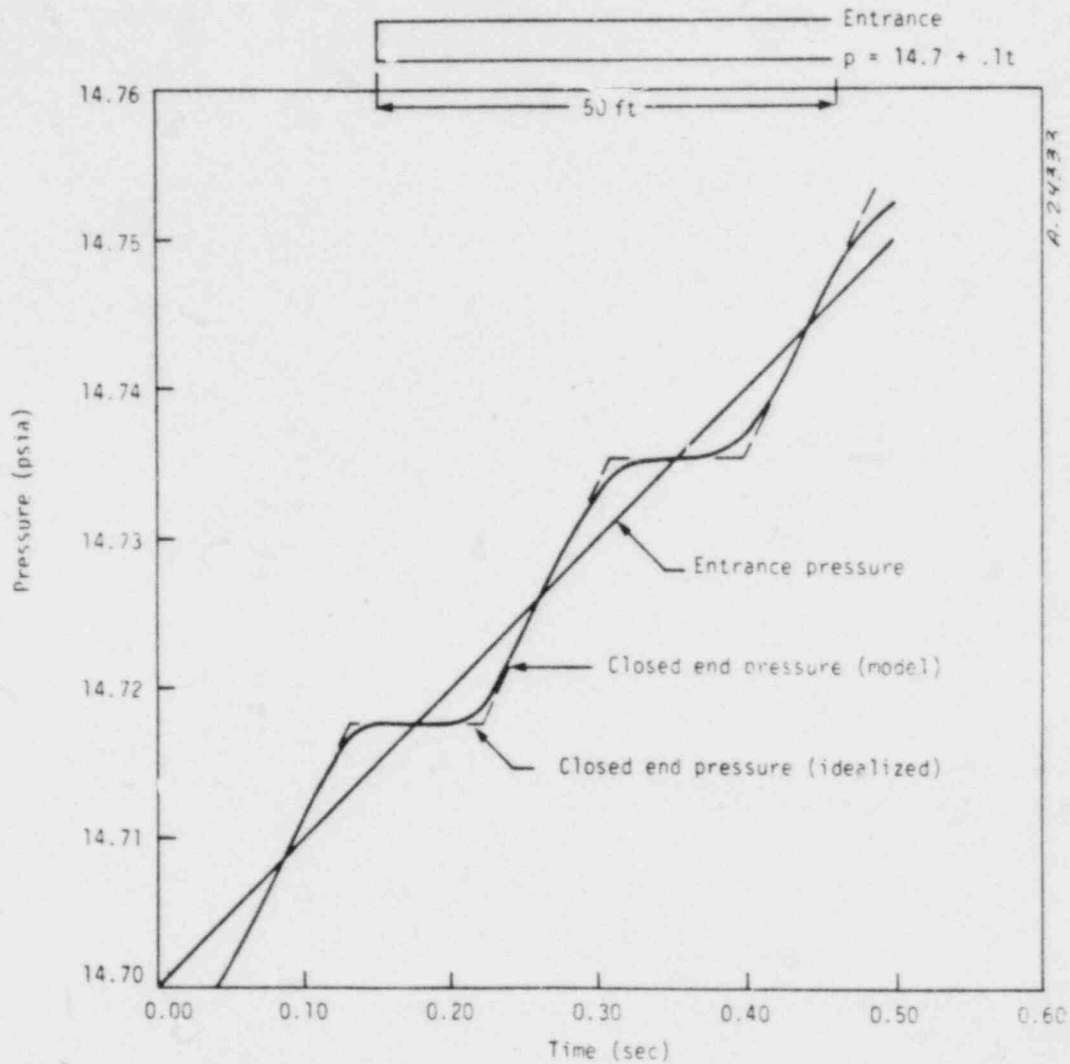
Figure 4-2. Test Case 3 -- transient ramp pressure at entrance to dead-end pipe.
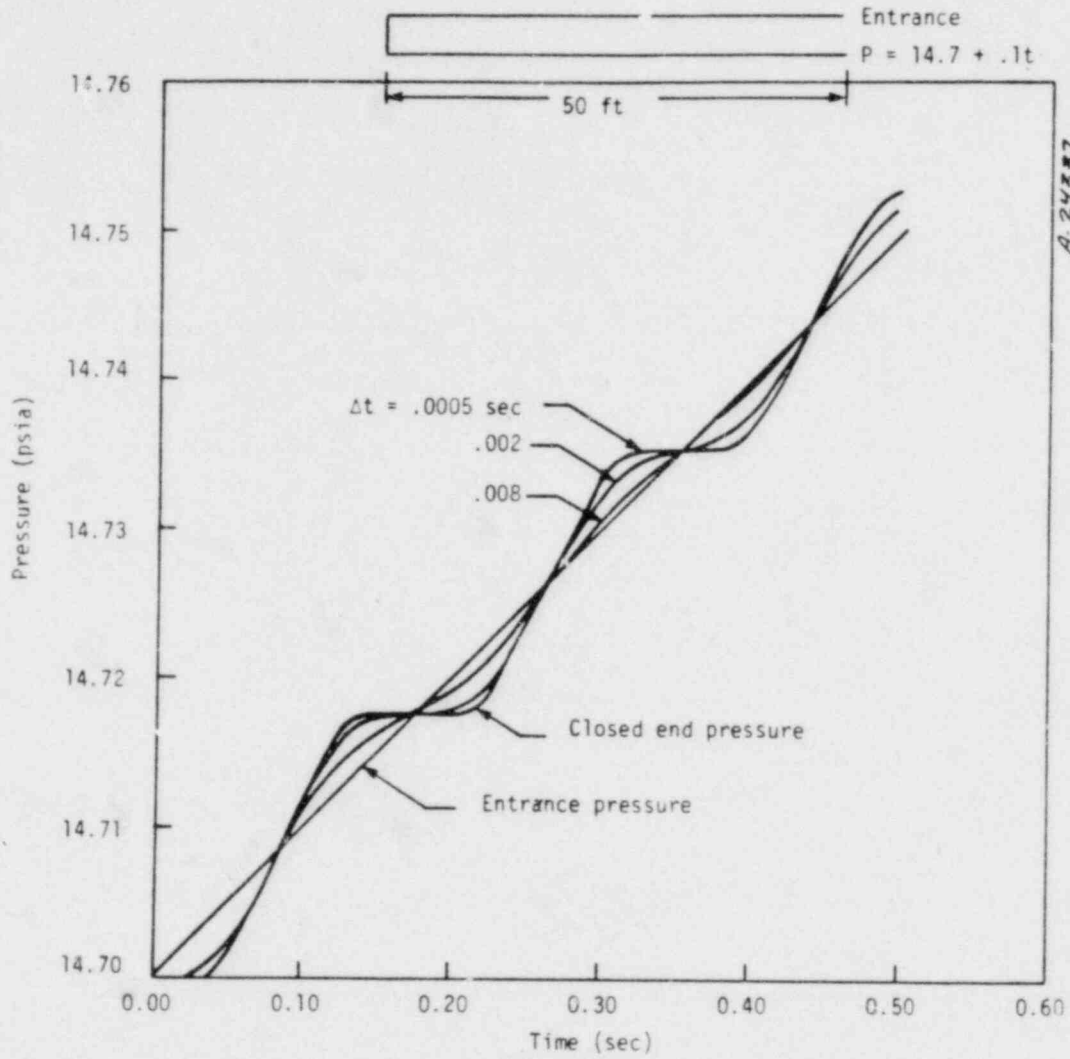
Figure 4-3. Test Case 4 -- timestep sensitivity.

Figure 4-2. Final selection of a reasonable timestep for the compressibility study required consideration of force and pressure sensitivity to timestep size in pool swell transients (Section 4.5).

5. Node Spacing Sensitivity -- Test case 3 was repeated with 11, 21, and 40 evenly spaced nodes along the 50 ft pipe at timestep sizes ranging from 0.0005 to 0.008 seconds. Program results were insensitive to variation in node spacing. The maximum disparity between 11-node and 40-node results was 0.0005 psi with 0.0005 second timesteps and became smaller as timestep size was increased.

4.3 DOWNCOMER WATER CLEARING

"Clearing" occurs as the waterleg which initially occupies the lower downcomer region is expelled into the pool. The dynamic relation which governs the slug clearing process (Figure 4-4) is a simple force balance which includes the vent exit node pressure, pool static pressure at the vent exit level, and gravity as forcing functions and uses the instantaneous slug mass (excludes water which has already entered the pool) plus a user-specified virtual mass (input as a volume) for the total mass being accelerated.

The downcomer has "cleared" when the downcomer waterslug has been completely expelled. In the model this is the same as when the bubble volume equals the initial slug volume; the new volume created by displacement of the water/air interface is assigned to the bubble. At each timestep the bubble volume and growth rate are checked against the initial waterslug volume. When the volume and growth rate are such

p. 24336
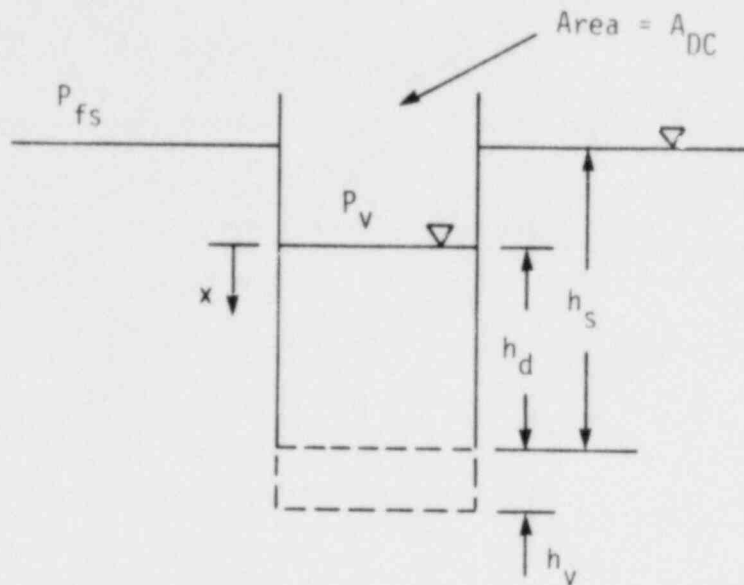
$$\left\{ P_V - P_{fs} - \rho(h_s - h_D + x) \right\} A_{DC} = \rho(h_D + h_v - x) A_{DC} \ddot{x} \qquad (4\text{-}15)$$

Figure 4-4. Downcomer clearing -- Governing Equation.

that the slug will be completely expelled in the next few timesteps, the program switches to the bubble dynamics equation.

4.4   BUBBLE MODEL -- GOVERNING EQUATIONS

Bubble continuity is calculated from the state equation in the form:

$$\dot{m}_B = \frac{d\left(\dfrac{P_B V_B}{R T_B}\right)}{dt} \qquad (4\text{-}16)$$

Energy equation options are:

$$P_B \dot{V}_B - \dot{m}_B c_p T_0 + \frac{d}{dt}\left(\frac{P_B V_B}{\gamma-1}\right) = 0 \quad \text{(adiabatic)} \qquad (4\text{-}17)$$

$$T_B = T_i \quad \text{(isothermal)}$$

The classic Rayleigh equation describing bubble dynamics in an infinite pool is given in terms of bubble radius as:

$$R\ddot{R} + \frac{3}{2}\dot{R}^2 = \frac{g_c}{\rho}\left(P_B - P_\infty\right) \qquad (4\text{-}18)$$

or in terms of bubble volume as:

$$\ddot{V}_B = \frac{4\pi g \sqrt[3]{\frac{3V_B}{4\pi}}}{\rho}\left(P_B - P_\infty\right) + \frac{1}{6}\frac{\dot{V}_B^2}{V_B} \qquad (4\text{-}19)$$

The new bubble model uses a modified Rayleigh equation:

$$\ddot{V}_B = \frac{\dfrac{4\pi g}{\rho}\sqrt[3]{\dfrac{3V_B}{4\pi}}\left(P_B - P_{fs} - \rho h_s\left(1 - \dfrac{\eta t}{h_s}\right)\right) + \dfrac{1}{6}\dfrac{\dot{V}_B^2}{V_B}}{\left(1 + \dfrac{\sqrt[3]{\dfrac{3V_B}{4\pi}}}{\phi}\right)\left(1 - \dfrac{\eta t}{h_s}\right)} \qquad (4\text{-}20)$$

where ϕ = wall proximity factor

η = bubble rise velocity

The term $1 + \dfrac{\sqrt[3]{\dfrac{3V_B}{4\pi}}}{\phi}$ causes $\ddot{V}_B$ to behave like a Rayleigh bubble

for small V_B and to behave like a slab bubble $(\ddot{V}_B \sim (P_B - P_\infty))$ for large V_B. The coefficient ϕ is a function of wall proximity. Its value is set when the model is 'tuned' against quarter scale test data. The term $(1 - \frac{nt}{h_s})$ causes the bubble stiffness to decrease with time to simulate bubble rise. η is adjusted to cause $\frac{nt}{h_s} = 1$ at bubble breakthrough.

The final boundary specification needed in the clearing and bubble model equations is the freespace pressure, calculated using a process exponent, n, as:

$$P_{fs} V^n_{fs} = \text{constant.} \qquad (4-21)$$

4.5 TIMESTEP AND NODALIZATION SENSITIVITIES

A 26-node model (Figure 4-5) vent system was used in a timestep sensitivity study. The test case used a full-scale vent system with mass flowrate specified at the inlet (368.4 lbm/sec). Vent flow was adiabatic, and the isothermal bubble option was used. Downcomer submergence was 4.248 ft; initial downcomer-to-freespace ΔP was zero. Figures 4-6 and 4-7 compare resulting pressures and torus forces from runs with timesteps of 0.0005, 0.002, and 0.008 seconds. Comparison of the curves confirms that 0.002 seconds is an adequately small timestep to achieve reliable results for the purposes of the compressibility study. Throughout the compressibility study, timesteps of 0.002 seconds were used in full scale runs and 0.001 seconds in quarter scale runs.

f1/D	NODE LENGTH (ft)	AREA (ft²)
		192.0
0	1.235	192.0
0	1.235	192.0
0	1.235	192.0
0	1.235	192.0
0	1.235	192.0
0	1.00	5.01
0	3.909	4.125
1.475	2.63	4.125
0.0096	2.63	4.125
0.0096	2.63	4.125
0.0096	2.63	4.125
0.0096	2.63	4.125
0.0096	2.63	4.125
0.0096	2.63	4.125
1.5038	1.63	4.125
0	1.00	4.084
1.079	2.50	4.084
0	0.30	5.83
0.0866	2.00	5.83
0.0866	2.00	5.83
0.0883	2.00	5.83
0	0.30	3.012
1.291	2.80	3.012
0.090	2.80	3.012
0.091	2.80	3.012
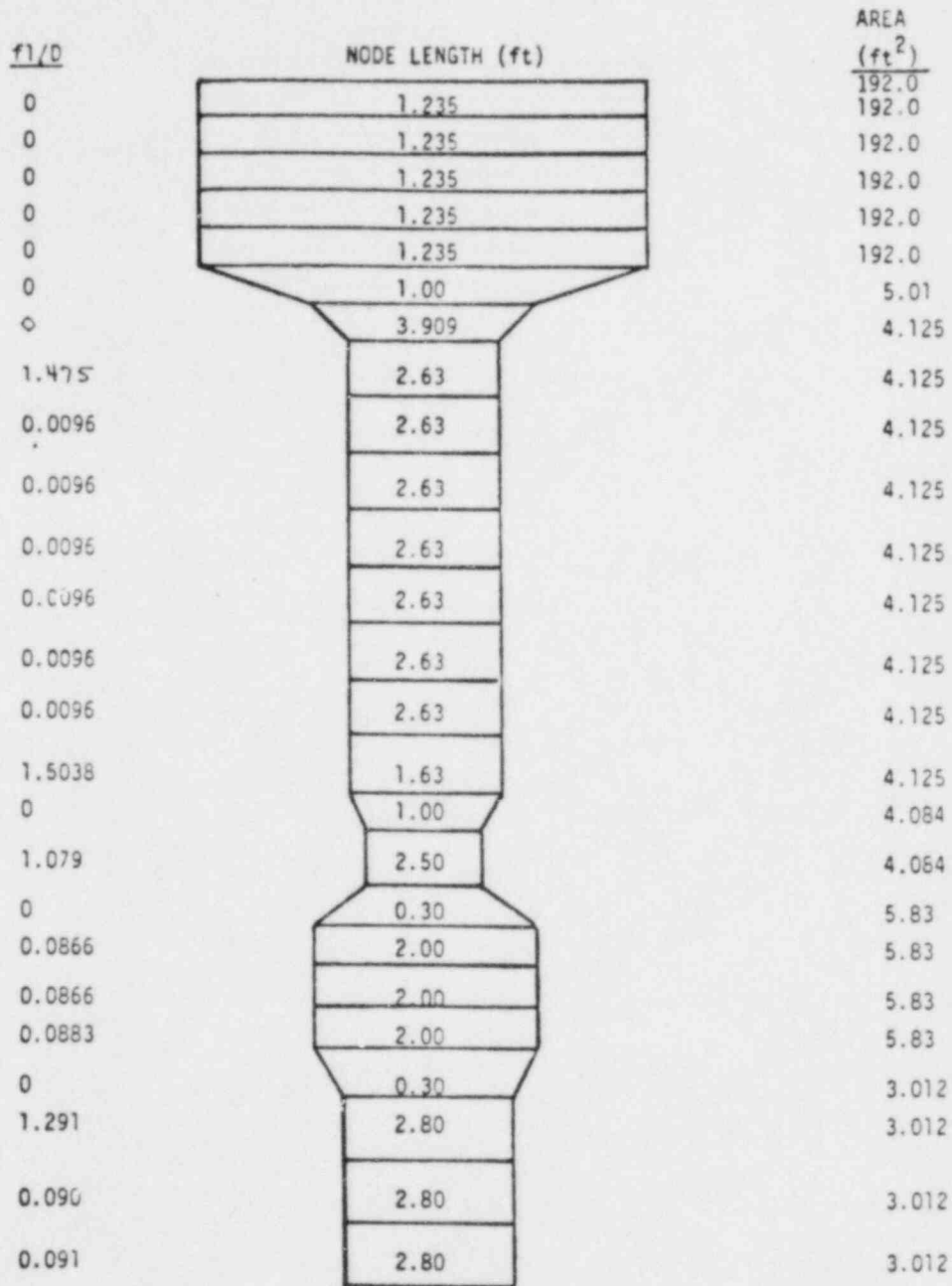
Figure 4-5. Full scale vent system -- 26-node configuration.
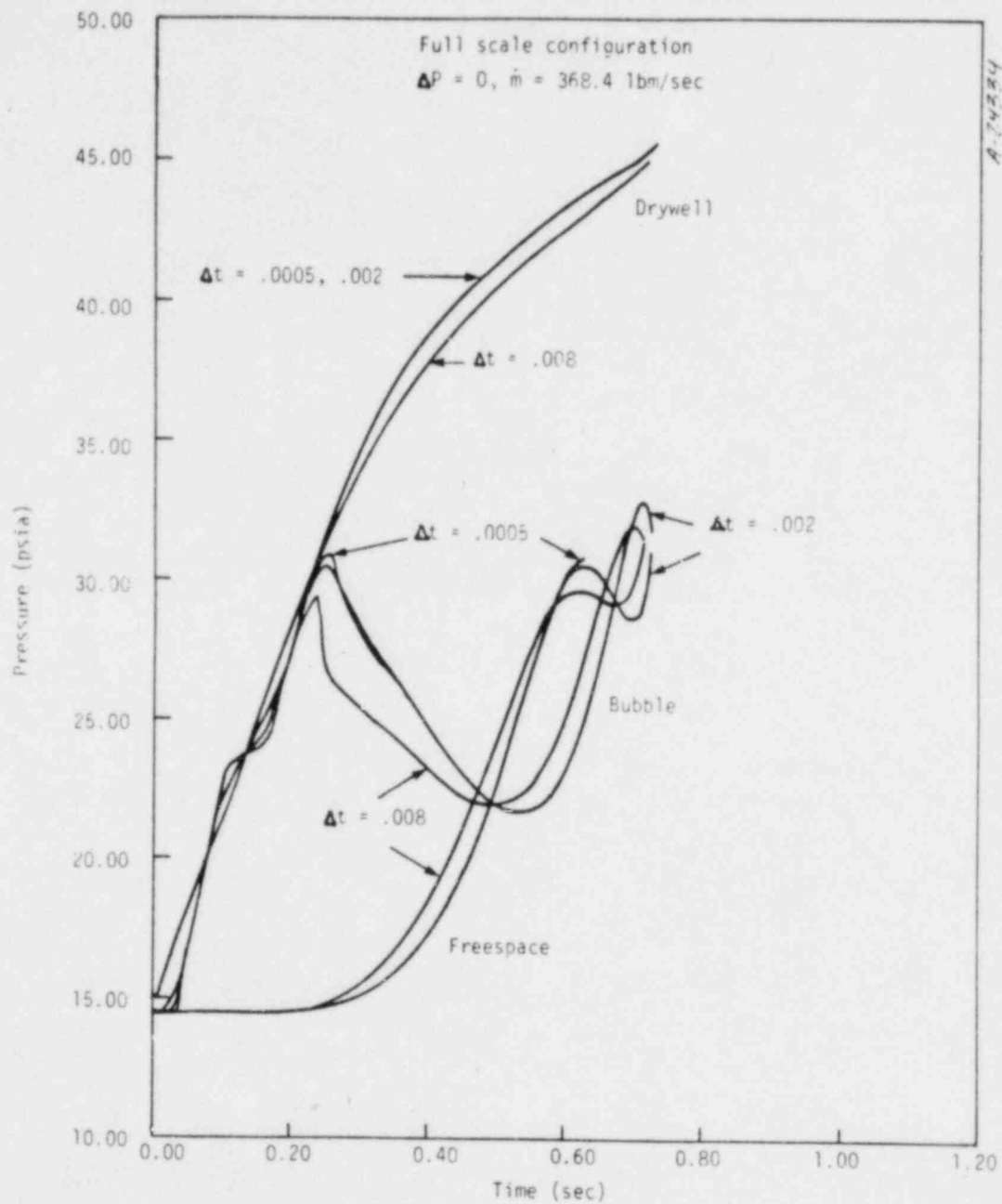
Figure 4-6. Timestep sensitivity -- pressures.
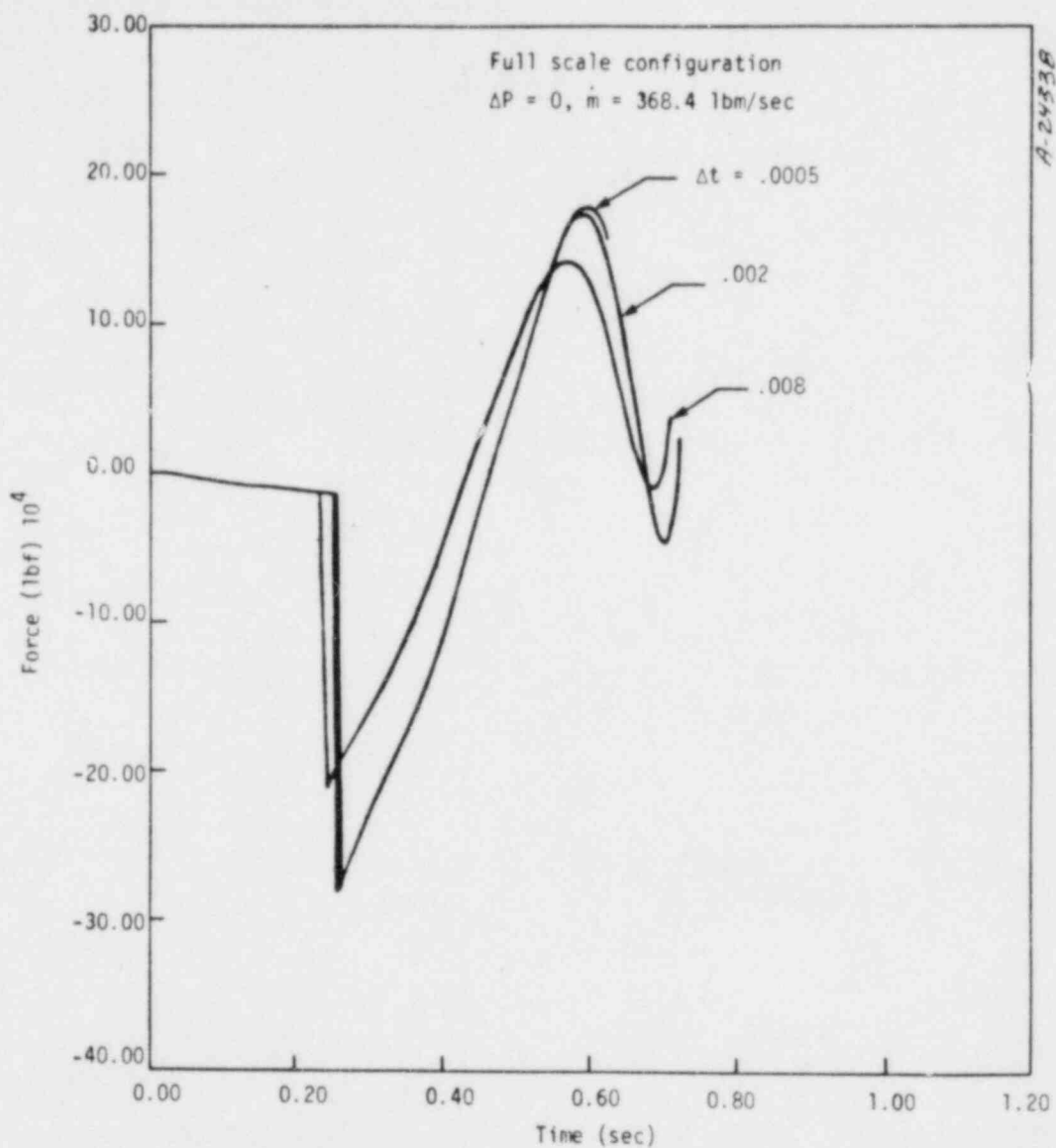
Figure 4-7. Timestep sensitivity -- force.

The same full scale mode was used in a nodalization sensitivity study. Results from the 26-node configuration (Figure 4-5), an 18-node configuration (Figure 4-8) and an 11-node configuration (Figure 4-9), are compared in Figures 4-10 and 4-11. Comparison of the curves indicates that the 26-node configuration, which was used in the full scale compressibility study cases, is more than adequate for the purposes of the study.
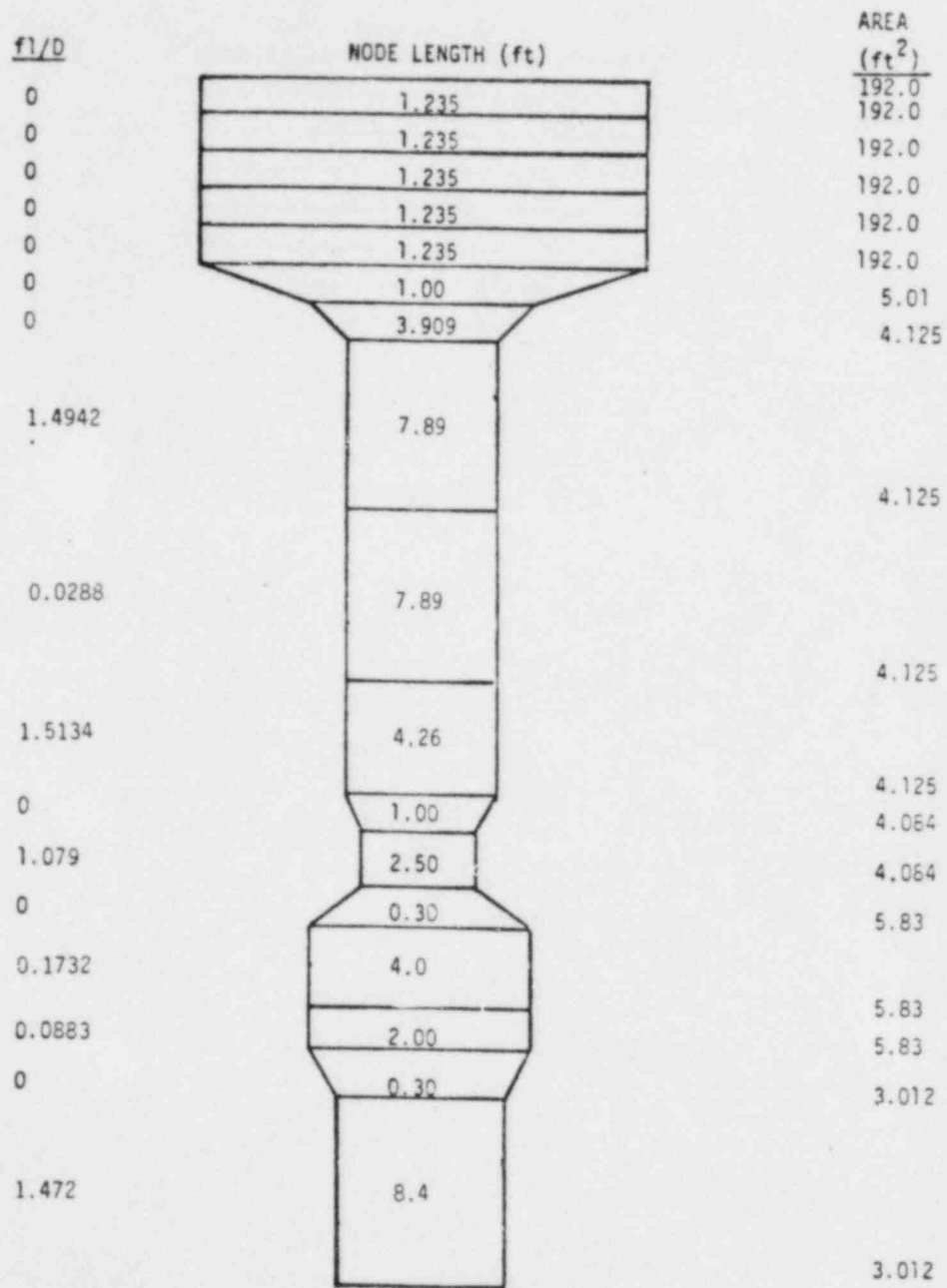
Figure 4-8. Full scale vent system -- 18-node configuration.

f1/D	NODE LENGTH (ft)	AREA (ft²)
0		192.0
0		
0	6.175	
0		
0		192.0
0	1.00	5.01
0	3.909	4.125
3.0364	20.04	
0	1.00	4.125
		4.064
1.079	2.50	4.064
0	0.30	5.83
0.2615	6.0	
		5.83
0	0.30	3.012
1.472	8.4	
		3.012
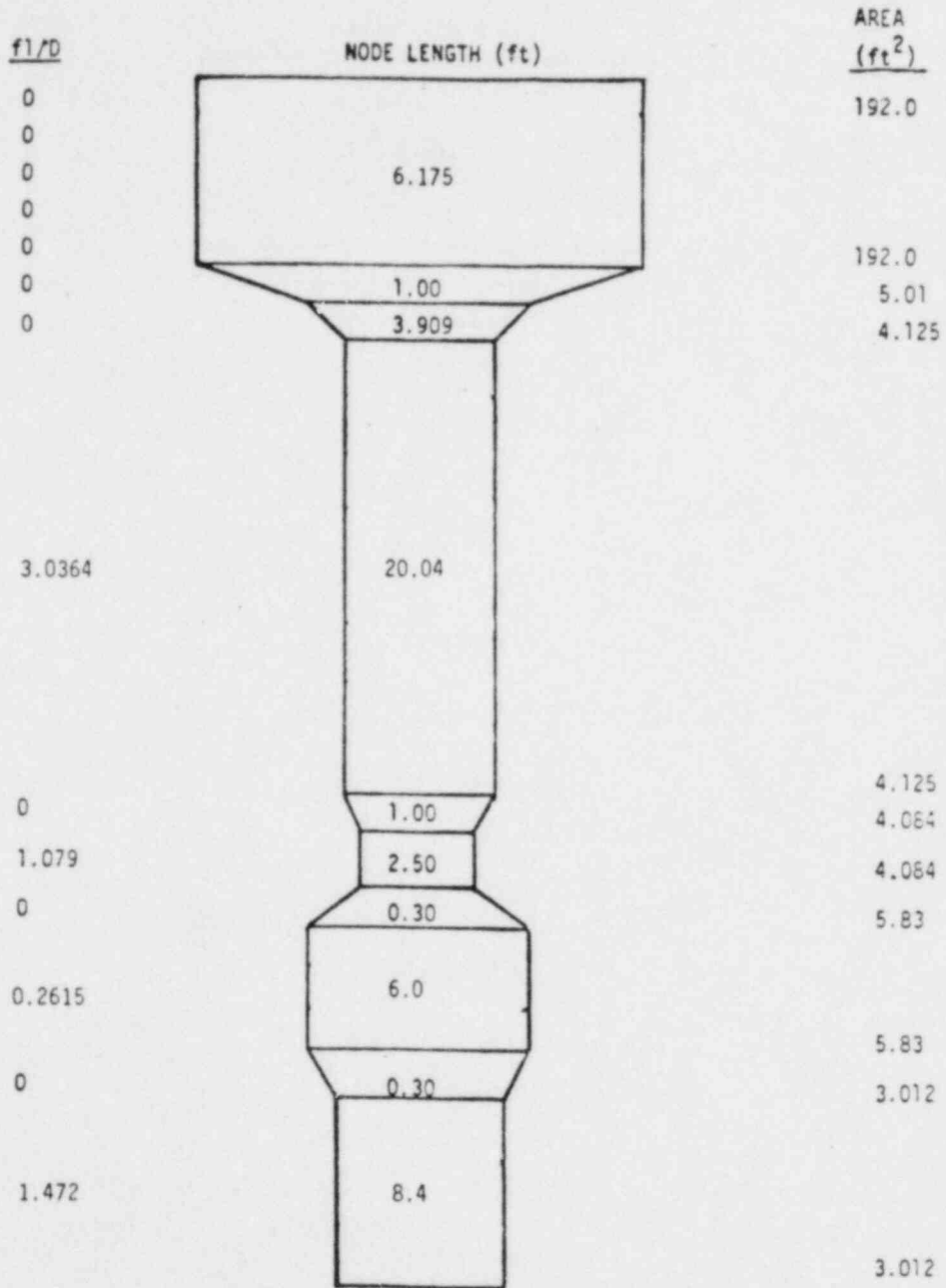
Figure 4-9. Full scale vent system -- 11-node configuration.
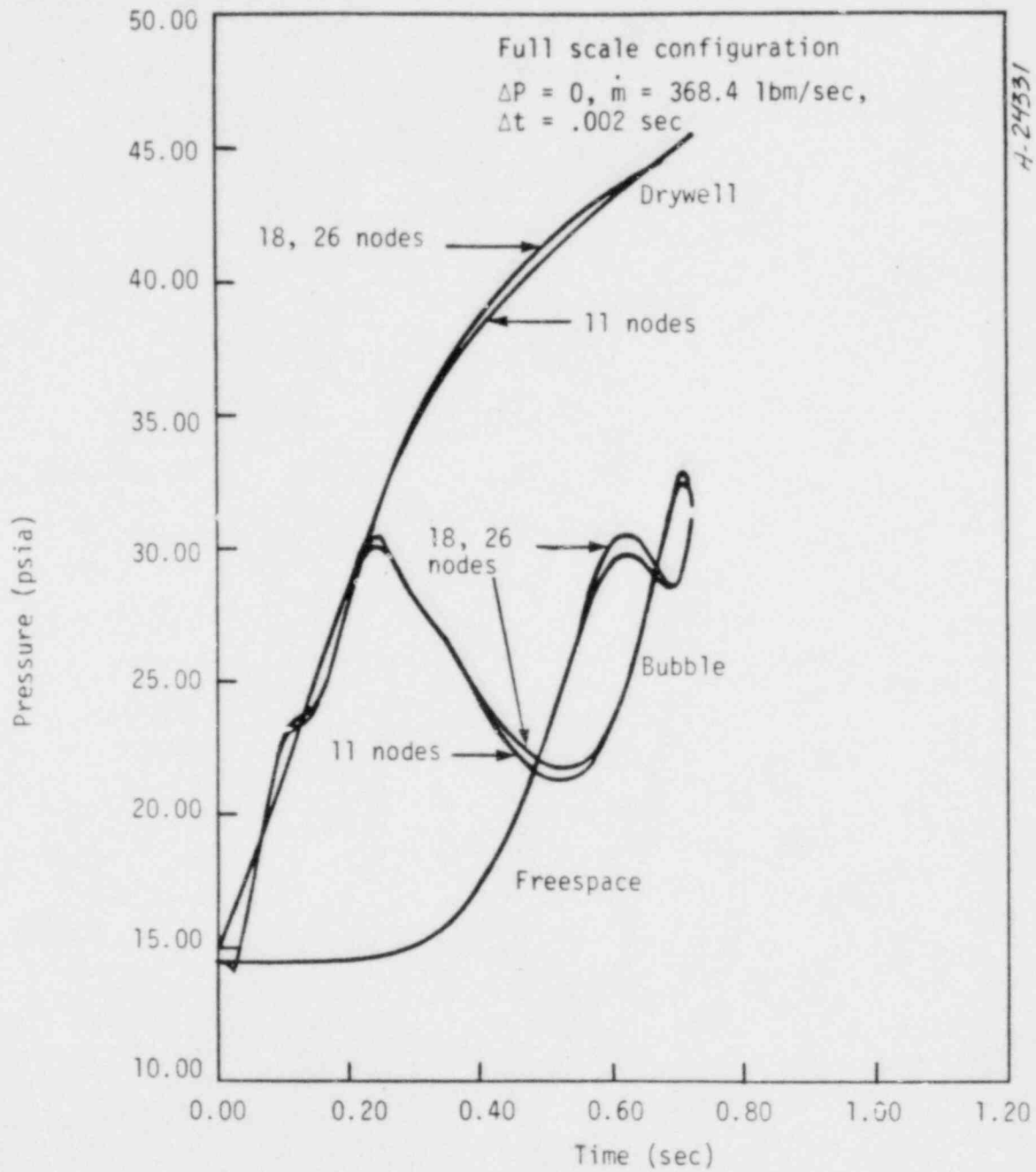
Figure 4-10. Nodalization sensitivity -- pressures.
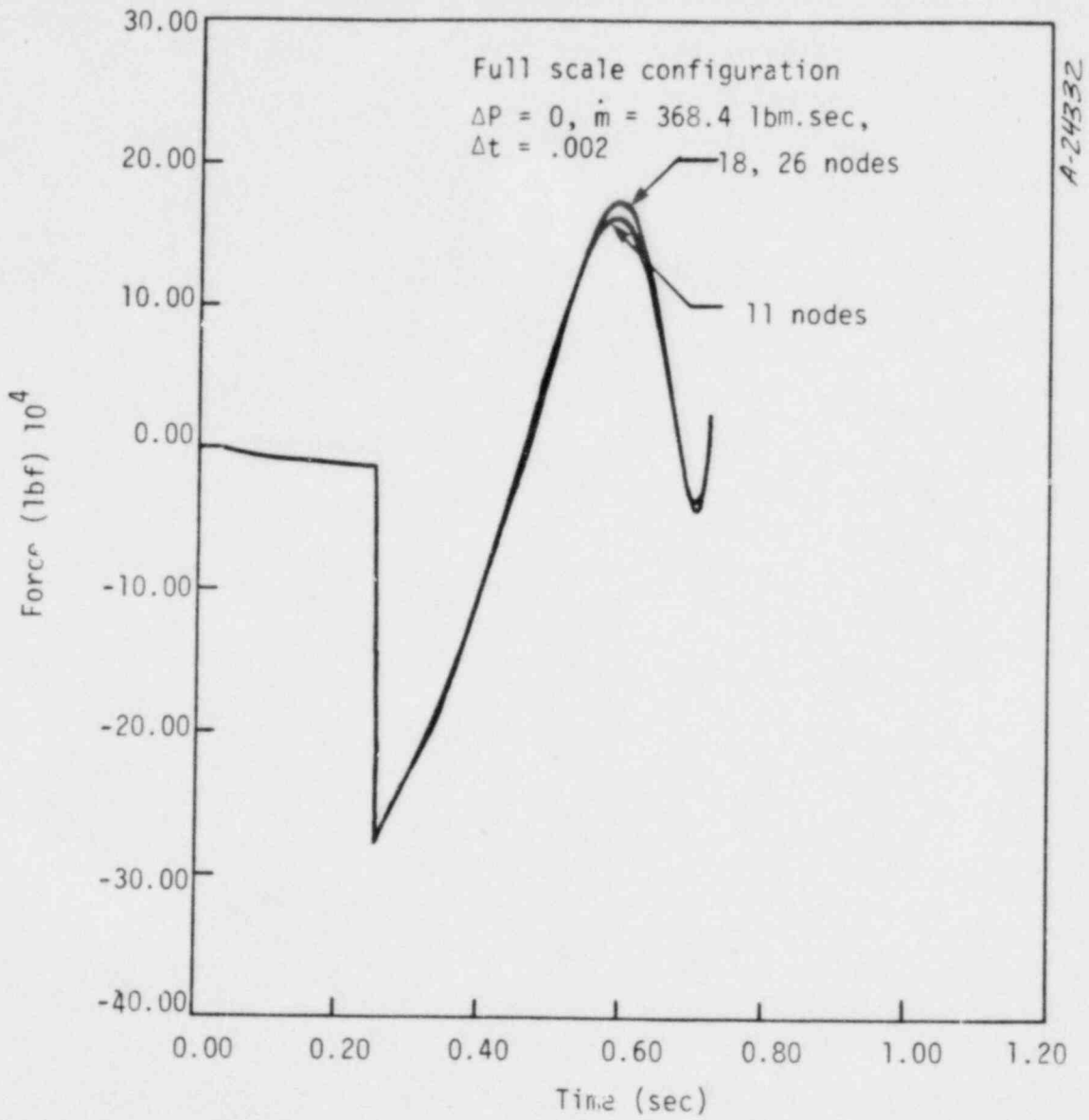
Figure 4-11. Nodalization sensitivity -- force.

SECTION 5

MODEL CALIBRATION AND QUALIFICATION

The various phases of the model evaluation are summarized in Table 5-1. First, the model was tuned against QSTF (as tested) data to find optimal selections for the heat transfer options and the two bubble model controls, ϕ and η. Further model qualification was obtained through comparison with EPRI/Chambré test and model results. Full Scale Test Facility (FSTF) data confirmed the model's performance with full size vent system dimensions and scaled-up bubble model controls. Finally, to quantify compressibility effects (Section 7), idealized ("perfect") QSTF test cases and the corresponding full scale cases were compared using the calibrated model and the Moody scaling relationships.

The calibration phase of the model evaluation used a 9-node representation of QSTF with flow resistances lumped at the two orifice locations (Figure 5-1). The Monticello configuration was used because the QSTF plant-unique Monticello test series covered the widest range of submergences (3 ft. 4 in. to 4 ft. 3 in.) and ΔP's (zero to full). Good agreement with test data was obtained over a wide range of ΔP and submergence by adjusting ϕ, the wall proximity factor. For a fixed submergence, ϕ is decreased as ΔP decreases; decreasing ΔP (longer waterleg) increases bubble pressure at clearing and drives the bubble deeper into the pool, increasing constraints on bubble growth (wall

effects). For a fixed ΔP/submergence (or fixed ΔP), ϕ is decreased with increasing submergence (longer waterleg); wall effects are greater since the bubble is injected deeper in the pool. Figure 5-2 shows that ϕ varies in a predictable and well-behaved manner over the range of test case conditions. Using a constant bubble rise velocity, r, of 4.75 ft/sec, the model agreed well with data for all the test cases. The model heat transfer option which gave the best agreement with test data was the adiabatic-vent/isothermal-bubble combination. Comparisons between QSTF data and calibrated model results for the four test cases are shown in Figures 5-3 to 5-5.

Bubble pressure comparisons (Figure 5-3) show good overall agreement. In the zero ΔP cases, the model slightly overpredicts bubble pressure at the time of clearing, probably because it does not adequately account for virtual mass effects of the vent waterslug. During the subsequent rapid bubble growth, bubble pressure in the model drops below the test data, then recovers more rapidly than the data. These deviations occur because the model simply forces the pool surface against the freespace air volume which is compressed until breakthrough occurs due to slug thinning. In the test, the pool surface hits the header/deflector while the bubble is still growing; bubble impedance changes, and heat transfer and turbulent mixing effects are introduced in the freespace, followed by bubble breakthrough. The model accounts for slug thinning, but does not treat mixing or thermal effects.

Drywell and freespace pressures (Figure 5-4) show excellent agreement with the data until late in the transient when noticeable differences occur in the freespace pressure. Again, this is because the complicated mixing effects which occur after vent header impact are not modeled.

Overall, the model matches the experimental load transients very well (Figure 5-5). At zero ΔP, the transition from vent clearing to the bubble model causes only a small departure from the data. Deviations late in time _ ? again evident; however, in general, peak upload is not strongly affected.

Next, the calibrated mode, was checked against EPRI/Chambré test and model results. Figure 5-6 shows the nodalizations used for subscale (small compressibility effects) and full scale simulations of the EPRI 1/11.7 scale test facility. The bubble model parameters, ϕ and η, determined from QSTF data comparison, were scaled down to 1/11.7 using Table 3-1 relationships. Model and test results are compared in Figure 5-7. Drywell and freespace pressures show good agreement; the model overpredicts bubble pressure somewhat. Chambré's analysis-to-experiment comparison (Figure 5-8) is almost identical. Note also that both analytical models show a time delay in the predicted bubble pressure.

To simulate full scale compressibility effects, Chambré reran his model as if the test had been run with Mach number scaling (Table 3-1) rather than resistance scaling: he reduced the vent system temperature by the scale factor (1/11.7) and removed the orifice flow resistances. Results are shown in Figure 5-9. The GE/Acurex model gave very similar results when an EPRI full scale case with distributed losses was set up (nodalization in Figure 5-6) and the results were scaled down to 1/11.7 (Figure 5-10). Note that prior to clearing the one-dimensional and three-dimensional models agree closely in their predicted acoustic delays and pressurization rates. This confirms the applicability of the GE/Acurex one-dimensional vent flow model in evaluating compressibility effects. Later time variations in results should be expected since Chambré used an expansion valid for early time in his bubble model.

Comparison with test data at full scale was obtained using data from test M8 of the Full Scale Test Facility (FSTF) tests (Reference 10). The vent system was modeled with losses distributed as shown in Figure 5-11. The drywell pressure history from the test was used to specify the vent entrance boundary condition, and the model predicted freespace and bubble pressures. Agreement with test data (Figure 5-12) was reasonable considering the completeness and limitations of the data since the FSTF tests were not pool swell tests, for instance:

1. Bubble pressure was not actually measured in the test. The nearest pressure measurement was near the downcomer mitre, where local flow conditions may have caused differences between actual bubble pressure and the measured downcomer pressure.

2. Complete vent system initial temperature distribution was not available, so the model initial conditions may have been inaccurate.

3. The nearest available drywell pressure measurement (used as input to the code) was some distance from the vent entrance. Hence there is uncertainty regarding the input drywell pressure-time history.

4. Steam or water droplets may be entering the vent during the latter portions of the pool swell transient. (Not checked in the test and not handled by the model.)

TABLE .-1. ANALYSIS INPUT PARAMETERS

	ϕ (ft)	η (ft/sec)	$\dot{m}_{Drywell}$ (Single D.C.) (lb/sec)	Submergence (ft)	$\dfrac{\Delta P}{Sub}$	Scale
QSTF as Tested						
Mont 2	0.40	4.75	4.50	1.19	0.53	0.2801
Mont 5	0.30	4.75	4.50	1.19	0.0	0.2801
Mont 11	0.60	4.75	4.50	0.941	1.0	0.2801
Mont 13	0.40	4.75	4.50	0.941	0.0	0.2801
EPRI 1/11.7	0.12	2.62	0.0708	0.283	0.0	0.0855
EPRI Full Scale	1.755	8.96	387.87	3.311	0.0	1.0
FSTF	2.14	8.975	Specified $P_{DW(T)}$	3.333	1.0	1.0
QSTF "Perfect"						
Mont 5	See Fig.	4.75	4.285	1.19	Various	0.2801
Mont 11	See Fig.	4.75	4.285	0.941	Various	0.2801
Full Scale						
Mont 5	See Fig.	8.975	368.4	4.25	Various	1.0
Mont 11	See Fig.	8.975	668.4	3.36	Various	1.0

NOTE:
1. Adiabatic drywell and vent, isothermal bubble
2. Freespace = 1.2
3. A_e/total projected area = 0.73
4. All runs at 530°R initial temperature except FSTF which had $T_{DW}(0) = T_V(0) = 750$°R
5. Virtual length at D.C. exit = 0.25 $D_{D.C.}$

FL/D	Length of Node (ft)	Area (ft^2)
		9.122
0	2.852	
		9.122
0	0.3	.2364
7.8	0.1	.2364
	0.3	1.154
0	3.9	
		1.154
0	0.3	.2364
5.2	0.1	.2364
0	1.7	
		.2364
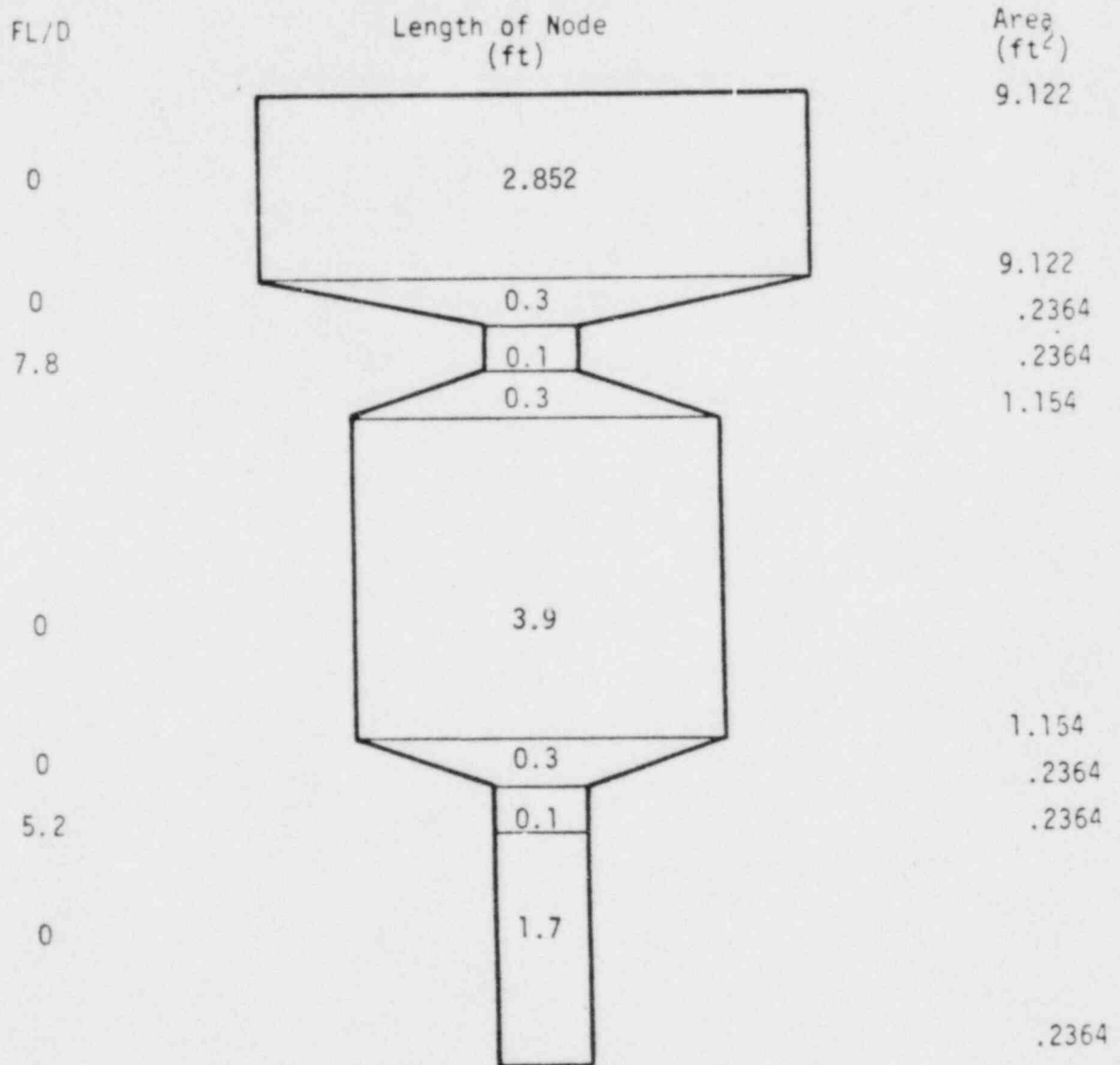
Figure 5-1. Nodal system -- CSTF "As Tested."

Calibration of Bubble Model
from Monticello QSTF
Data
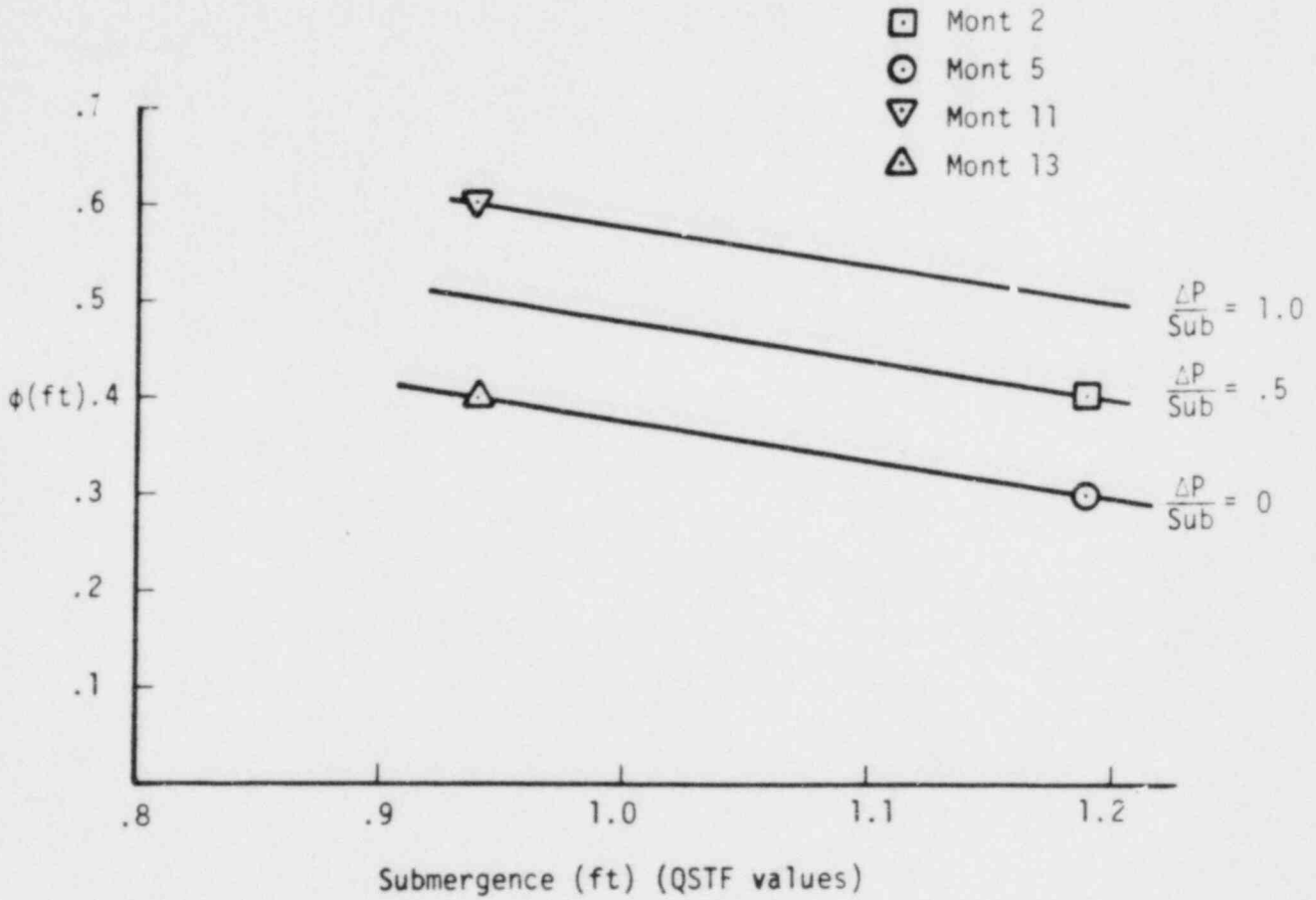
Figure 5-2. Wall proximity factor -- dependence on submergence and ΔP.

Figure 5-3. Model calibration -- bubble pressure comparison.

Figure 5-4. Model calibration -- drywell and freespace pressure comparison.

*General Electric Company proprietary information has been deleted.

*

Figure 5-5. Model calibration -- torus force comparison.

*General Electric Company proprietary information has been deleted.

A-24008

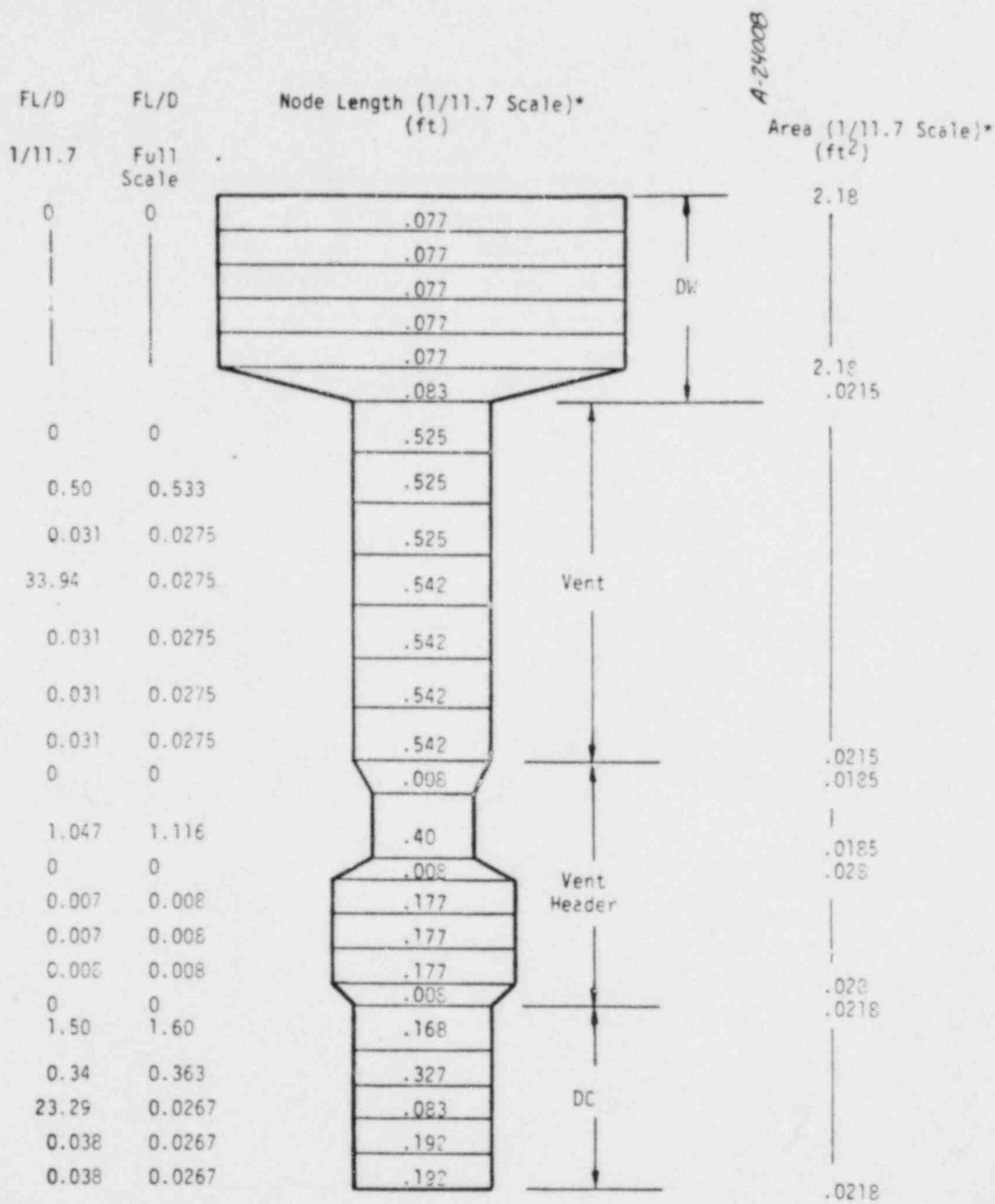| FL/D	FL/D	Node Length (1/11.7 Scale)* (ft)		Area (1/11.7 Scale)* (ft²)
1/11.7	Full Scale			
0	0	.077		2.18
		.077		
		.077	DW	
		.077		
		.077		2.18
		.083		.0215
0	0	.525		
0.50	0.533	.525		
0.031	0.0275	.525		
33.94	0.0275	.542	Vent	
0.031	0.0275	.542		
0.031	0.0275	.542		
0.031	0.0275	.542		
0	0	.008		.0215 / .0185
1.047	1.116	.40		.0185
0	0	.008	Vent Header	.028
0.007	0.008	.177		
0.007	0.008	.177		
0.008	0.008	.177		
0	0	.008		.028
1.50	1.60	.168		.0218
0.34	0.363	.327		
23.29	0.0267	.083	DC	
0.038	0.0267	.192		
0.038	0.0267	.192		.0218

$$*L_{FS} = 11.7(L_{1/11.7}), \quad A_{fs} = (11.7)^2 (A_{1/11.7})$$

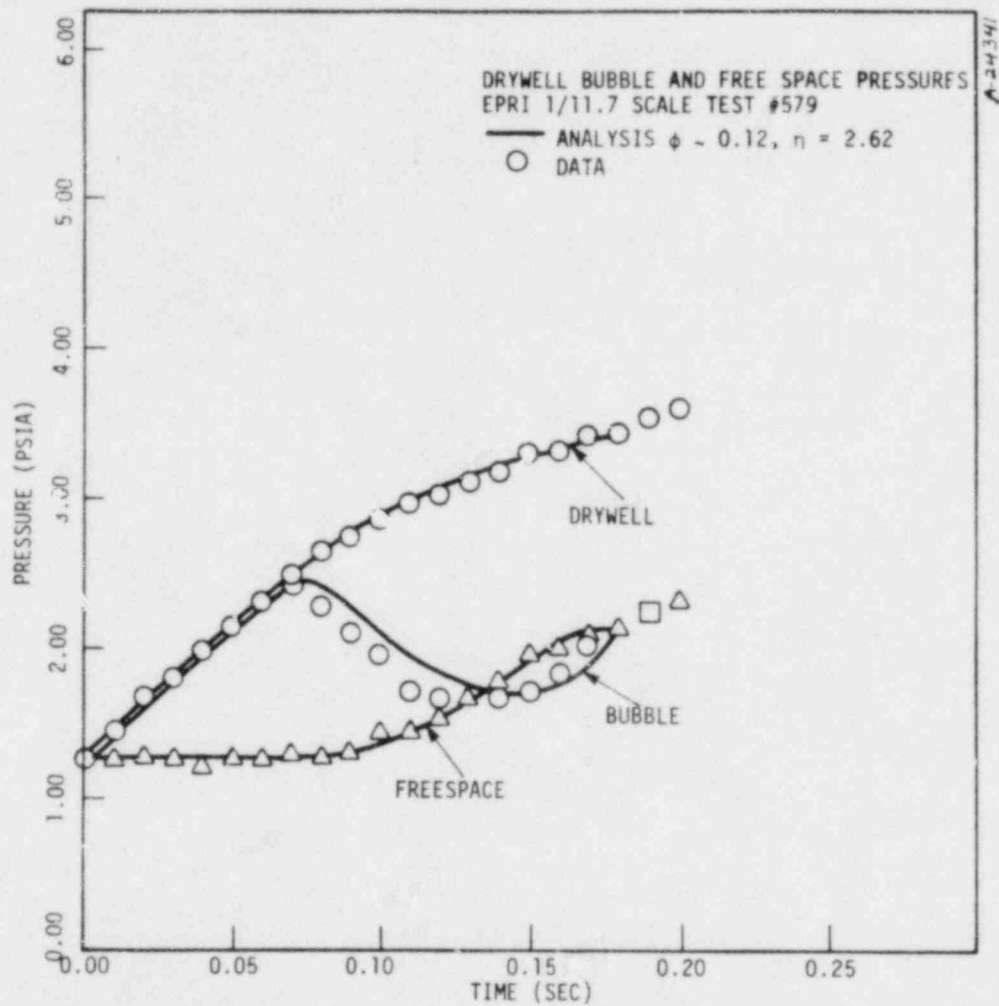Figure 5-6. EPRI nodal systems -- 1/11.7 and full scale.

Figure 5-7. Drywell bubble and freespace pressures (EPRI 1/11.7).
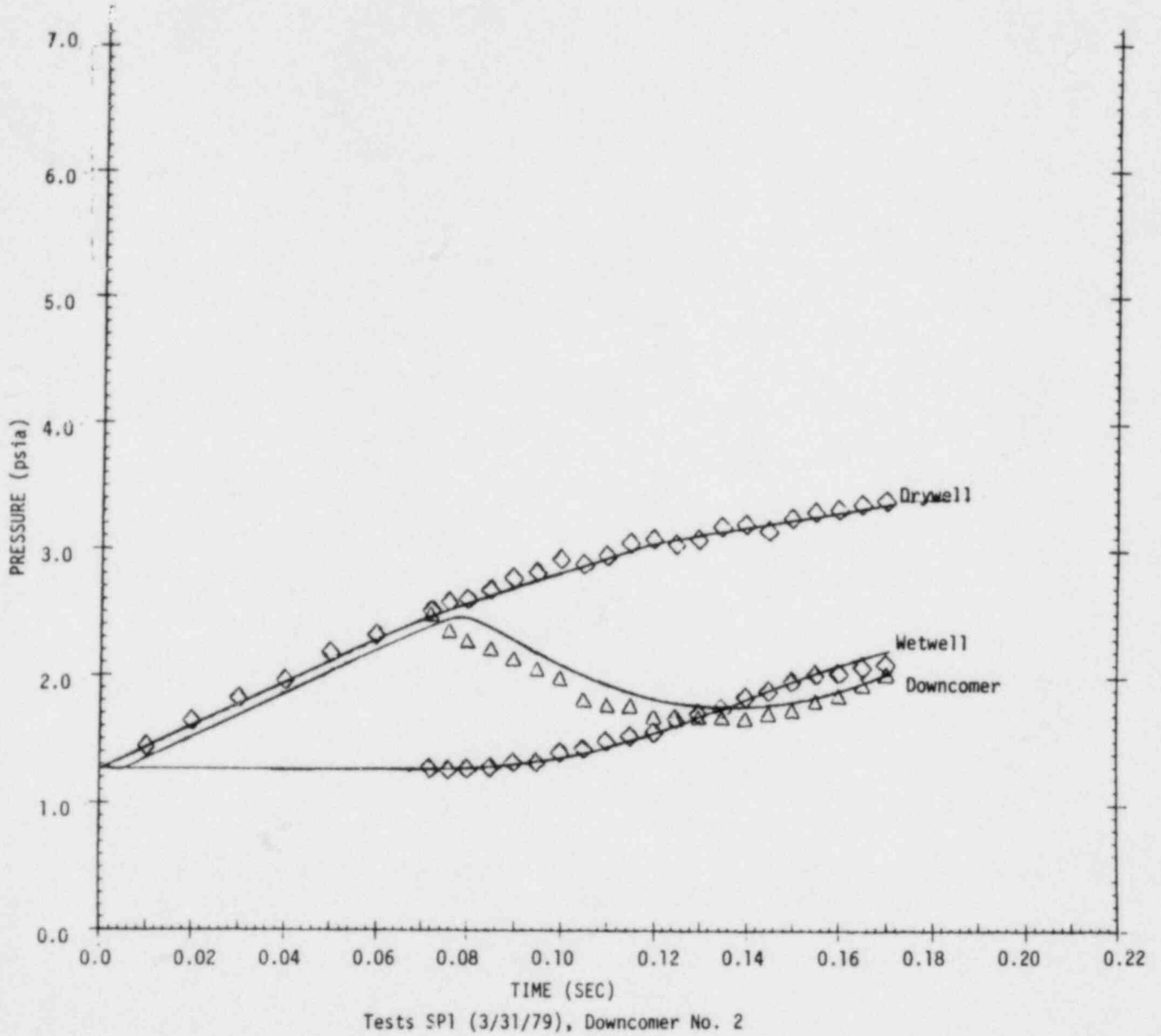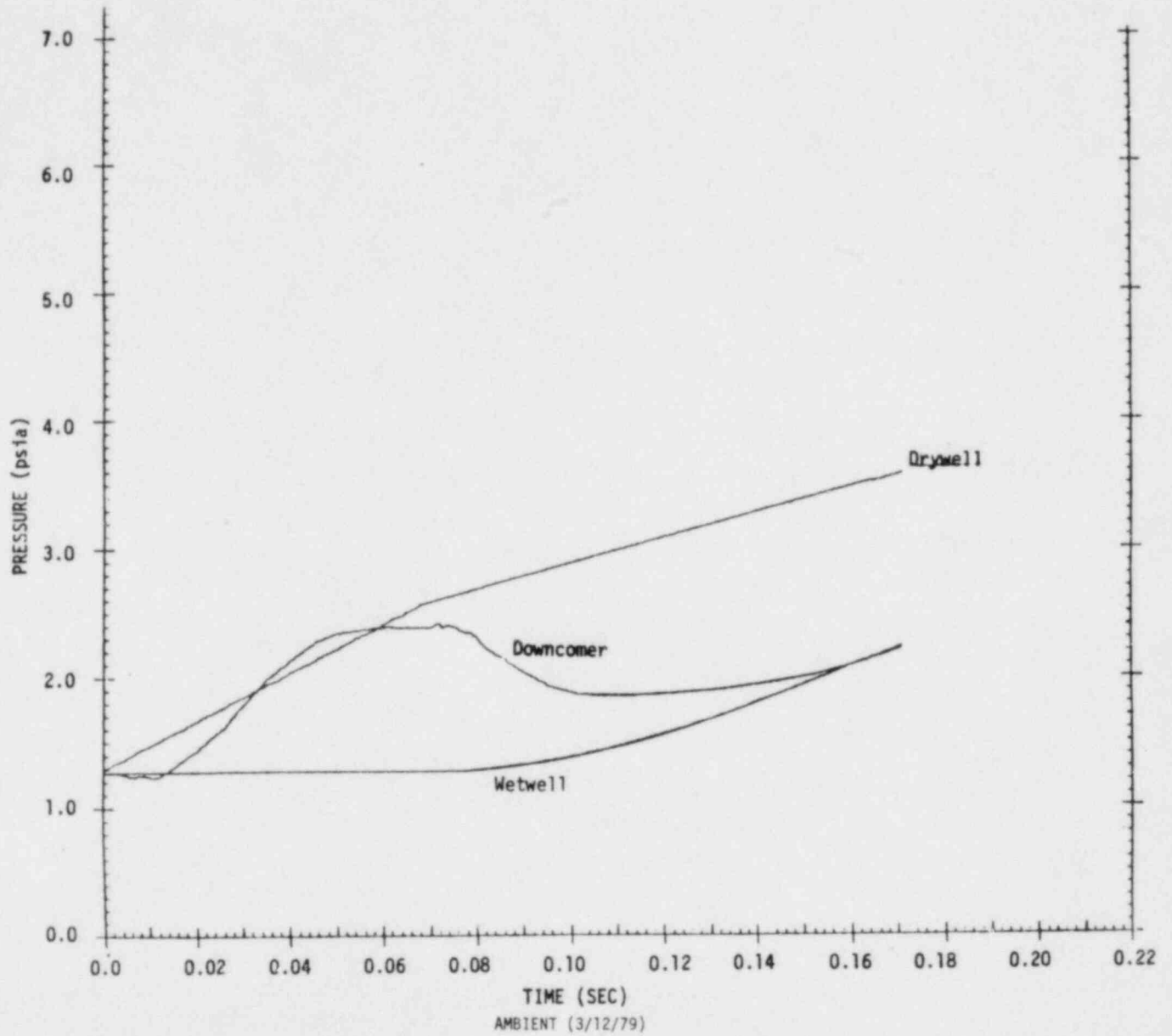
Figure 5-8. Chambre analysis -- 1/11.7 scale.

Figure 5-9. Chambre analysis -- full scale compressibility.
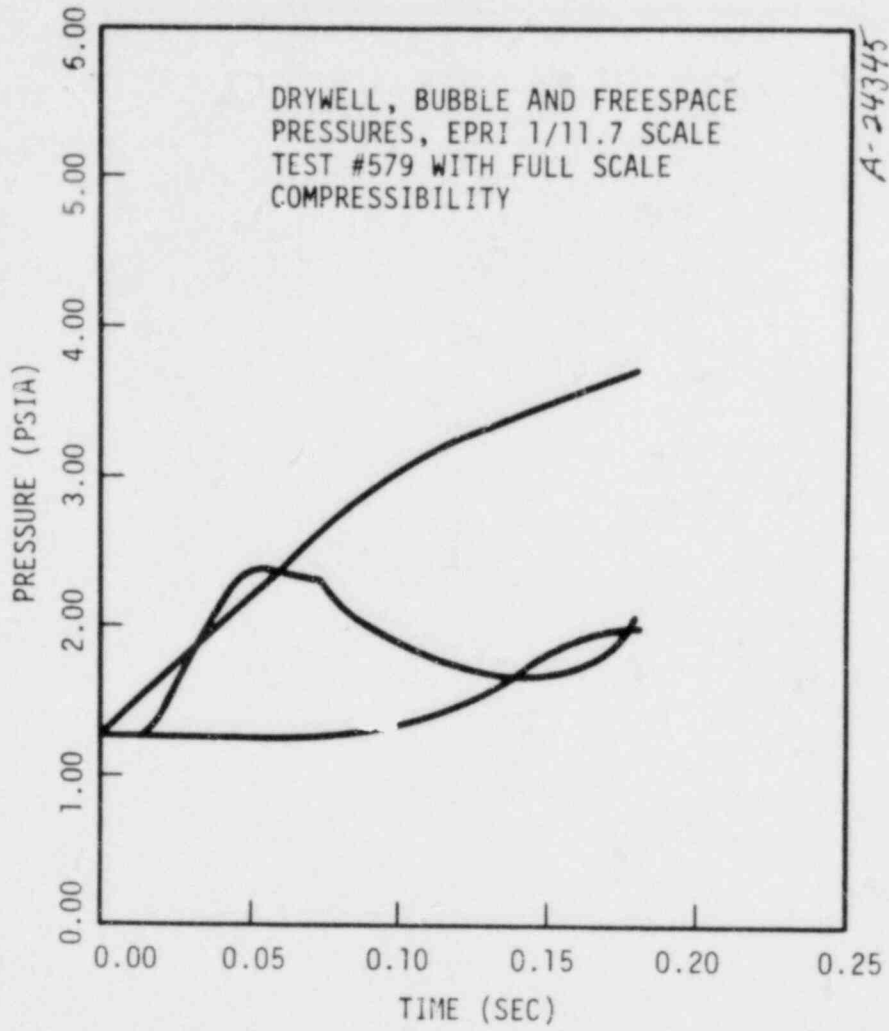(Simulated at 1/11.7 using scaled gas temperature)

DRYWELL, BUBBLE AND FREESPACE
PRESSURES, EPRI 1/11.7 SCALE
TEST #579 WITH FULL SCALE
COMPRESSIBILITY

A-24345

Figure 5-10. Acurex results -- EPRI system with full scale compressibility.

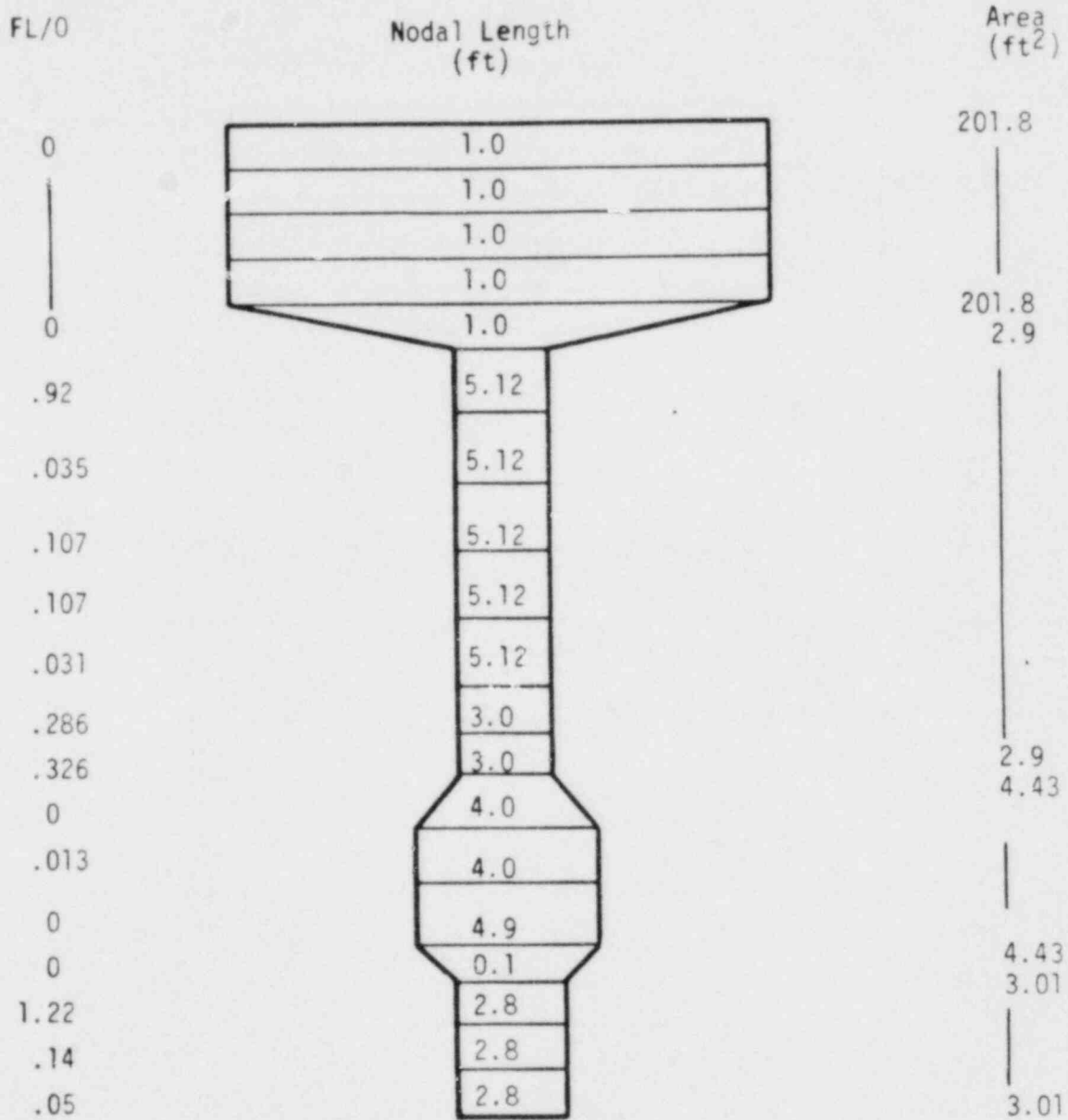| FL/0	Nodal Length (ft)	Area (ft²)
0	1.0	201.8
	1.0	
	1.0	
	1.0	
0	1.0	201.8 / 2.9
.92	5.12	
.035	5.12	
.107	5.12	
.107	5.12	
.031	5.12	
.286	3.0	
.326	3.0	2.9 / 4.43
0	4.0	
.013	4.0	
0	4.9	
0	0.1	4.43 / 3.01
1.22	2.8	
.14	2.8	
.05	2.8	3.01

Figure 5-11. FSTF nodal system.

Figure 5-12. Drywell, bubble and freespace pressures (FSTF -- test M8).

*General Electric Company proprietary information has been deleted.

SECTION 6

ANALYSIS -- COMPRESSIBILITY EFFECTS

Vent flow compressibility effects are manifestations of the finite pressure signal speed in the vent system. Prior to clearing, the vent exit pressure and pressurization rate oscillate about the drywell pressure ramp as pressure waves travel back and forth between the drywell and the vent exit. Following vent clearing, acoustic delays act to retard the developing vent exit flow. The GE/Acurex model was used to develop a better understanding of these effects and to aid in the interpretation of model predictions of Mark I compressibility effects.

Two simplified cases were run to demonstrate compressibility effects on mass flowrate at the vent exit. A prototypical full scale vent system and the corresponding resistance-scaled quarter scale system (1/4 the full scale lengths, 4 times the full scale flow resistance) were analyzed using the two sets of boundary conditions shown in Figure 6-1. Constant vent exit pressures, 15 psi in full scale and 3.75 psi in 1/4 scale, were used to simulate exhausting directly to atmosphere, thus eliminating vent clearing and pool dynamics effects. Temperature was not scaled (same as QSTF tests).

Case A applied a pressure ramp at the vent system inlet with all nodes initially at the exit pressure. Case B started with all nodes at 20 psi (5 psi at 1/4 scale), and initiated the transient with a step

decrease of the vent exit pressure, simulating an exit rupture disk. Results were compared at quarter scale; full scale flowrates and times were scaled down using the relationships in Table 3-1.

In the ramped inlet pressure case (Case A), the quarter scale flowrate shows one half the full scale time delay and responds more quickly to the pressurization (Figure 6-2). The time delay discrepancy occurs because Moody scaling shrinks the time scale by $SF^{1/2} = 1/2$, while the acoustic delay actually decreases by SF (as length) if acoustic speed is the same in both cases. Case B (Figure 6-3) has the same general characteristics; the full scale flowrate shows slower response than the quarter scale result. Also, there is a factor of 2 discrepancy in the initial flowrates resulting from scaling inconsistencies. Consistent scaling of transient compressible pipe flow would preserve Mach number at geometrically similar locations at corresponding values of nondimensional time ($t^* = t \sqrt{g/D}$). If temperature is not scaled, then preserving Mach number requires that $V_{model} = V_{prototype}$ at corresponding locations and times. Thus

$$\dot{m} = \rho VA \sim (SF)(SF^2) = SF^3$$

Moody scaling, based on steady flow, calls for $\dot{m} \sim SF^{7/2}$ (Table 3-1). The discrepancy during the acoustic wave dominated part of the transient is $SF^{1/2}$ (a factor of 2 for quarter scale) which is consistent with the Figure 6-3 result. The small (and conservative) discrepancy later in time results from FL/D scaling in compressible flow causing $\dot{m}$ not to vary precisely as $SF^{7/2}$.

The relative retardation of the developing full scale flowrate in the study cases is a very important compressibility effect -- it shows that scaling up QSTF results with the Moody scaling relationships gives

significantly larger than prototypical mass/energy injection into the suppression pool during the early part of the pool swell transient. This transient mass decrement introduces a significant conservatism into the evaluation of compressibility effects and is fundamental for understanding the Mark I load sensitivities presented in Section 7.

Three primary compressibility effects have been identified which can be used to predict trends in compressibility effects on pool swell loads: 1) compressibility effects delay the start of pressurization at the vent exit; 2) prior to vent clearing, the exit pressure and pressure rate oscillate about the drywell pressure ramp; 3) following vent clearing, acoustic delays (compressibility effects) cause a significant transient mass flow decrement before the vent exit reaches quasi-steady flow. This report evaluates compressibility in terms of its effects on three primary pool swell loads, download, download impulse, and upload.

Peak download occurs at the time of maximum bubble pressure, soon after vent clearing. Maximum bubble pressure occurs when the volumetric growth rate of the bubble exceeds the ability of the vent system flow to maintain the bubble pressure; it is sensitive to all three compressiblity effects. A high exit pressure at vent clearing promotes a high download, as does a high pressurization rate. However, compressibility effects cause the exit pressure and pressure rate to either increase or decrease relative to their incompressible values (the drywell values), depending on where the travelling wave fronts are in the vent system. Waterslug velocities during the clearing transient are low compared to sonic velocity in the vent, so the waterslug acts much like a closed end at the vent exit; prior to clearing, the vent exit pressure (really the pressure at the air-water interface) exhibits the response characteristics shown in

Test Case 3 (Section 4-2). There is no response for one wave travel time after which the pressure rate is twice the drywell rate for two wave travel times, and so on. The vent exit pressure rate cycles every four wave travel times or once every acoustic period, λ, defined as 4 x (vent length)/acoustic speed. Vent exit pressure oscillates at the drywell pressure as described in Figure 6-4. Peak download is affected by where the exit pressure is on its zig-zag path at the time of clearing.

A rarifaction wave returning from the drywell at or just after clearing turns the bubble pressure around rapidly, a mitigating effect on download. Since clearing time (and the number of acoustic periods before clearing) changes with waterleg length, the net compressibility effect on download might be expected to be cyclic, the most severe cases occurring when the waterleg length is such that peak bubble pressure occurs at conditions of high exit pressure and pressure rate.

With the GE/Acurex model set up in the full scale Monticello configuration with 3 ft. 4 in. submergence and a prototypical drywell pressurization rate, runs were made to determine clearing time as a function of waterleg length. Results and evident trends are indicated in Figure 6-5. The curve must always pass through the point (0, .25) since a zero-waterleg case clears after one wave pass (.25 λ). Using a higher drywell $\dot{P}$ rotates the curve clockwise slightly; clearing times are shorter for similar vent and waterleg lengths. For a plant with a shorter vent system, the acoustic period is smaller, so more acoustic periods will have elapsed at the time of clearing.

Based on the Monticello curve in Figure 6-5, Figure 6-6 indicates where clearing occurs in the vent exit pressure transient for various waterleg lengths. Figure 6-6 shows that even a small waterleg (a few

inches) delays clearing enough to avoid most of the initial double-$\dot{P}$ region. (All Mark I's were tested with waterlegs of at least 6 inches.) Curves similar to that of Figure 6-4 could be constructed for each Mark I plant, but they would be close to Monticello's, particularly near the origin, which turns out to be the only region of non-conservatism in evaluating compressibility effects on download (Section 7).

Peak upload occurs later, at the time of maximum pool deceleration, and is primarily controlled by the integrated mass flow into the bubble. Therefore, the conservative compressibility mass decrement effect is expected to be the dominant compressibility effect on peak upload. The cyclic response of downcomer clearing pressure with downcomer waterleg should be largely washed out by the time of peak upload.

Maximum pool velocity is determined by the download impulse (torus force integral during the download portion of the pool swell transient). The download impulse is a function of both the peak download and the mass flowrate entering the bubble following peak download. Therefore, compressibility effects on maximum pool velocity (or download impulse) are expected to fall between the effects calculated for peak download and peak upload.
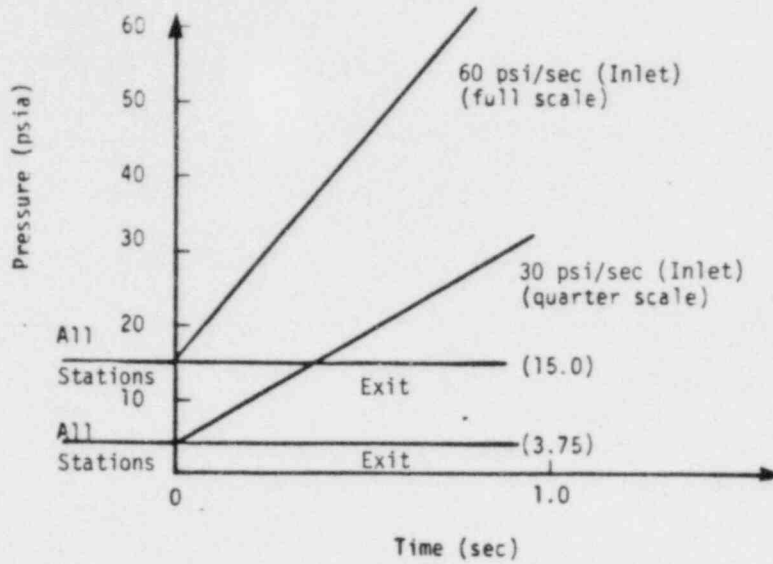
Test Case A. Ramp pressure increase at entrance.

Simplified Vent Model
Initial and Boundary Conditions
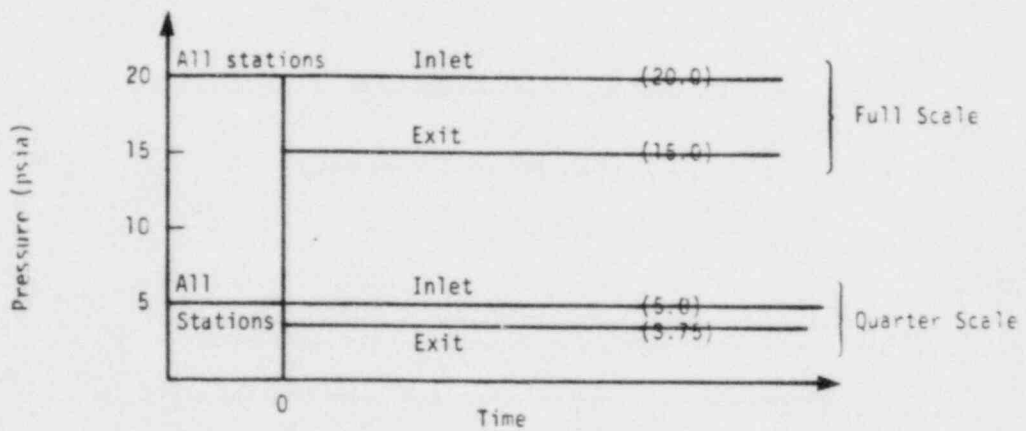
Test Case B. Step change in exit pressure.

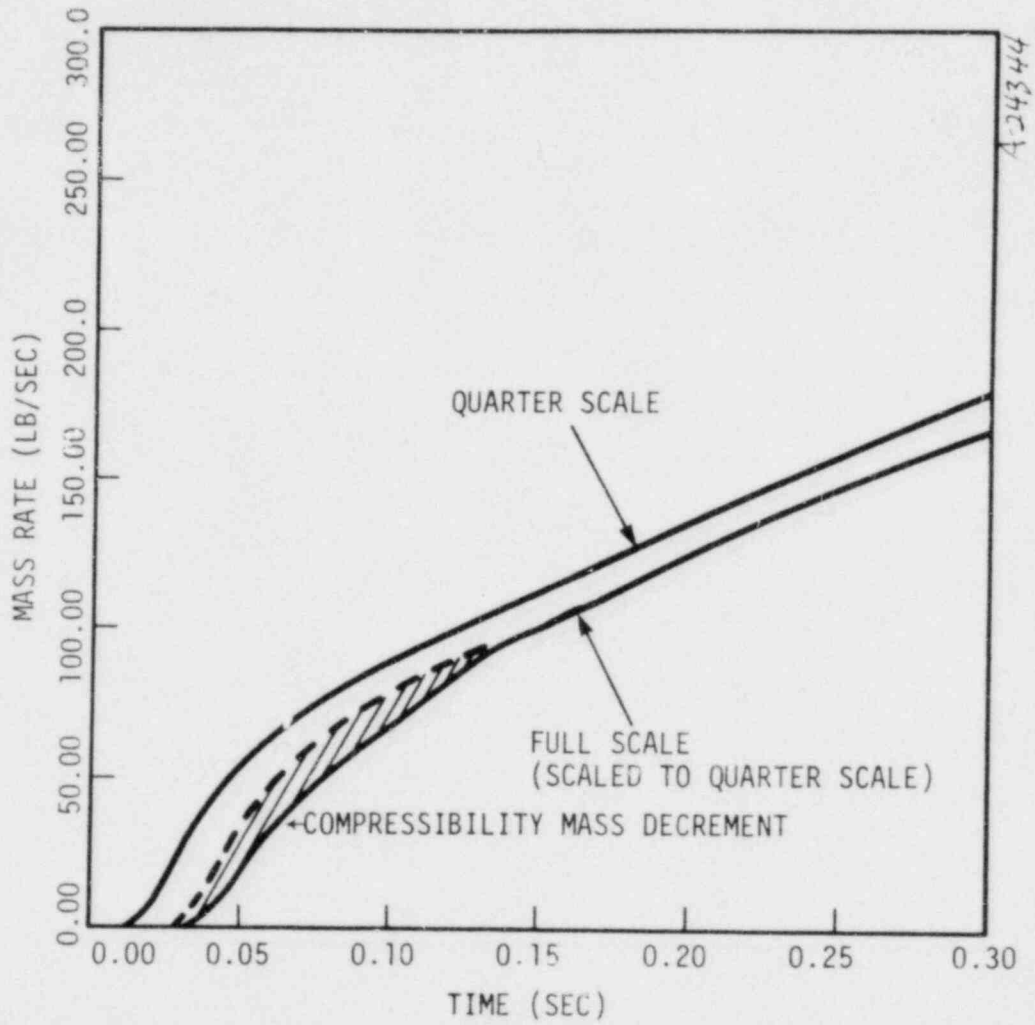Figure 6.1 Compressibility study cases.
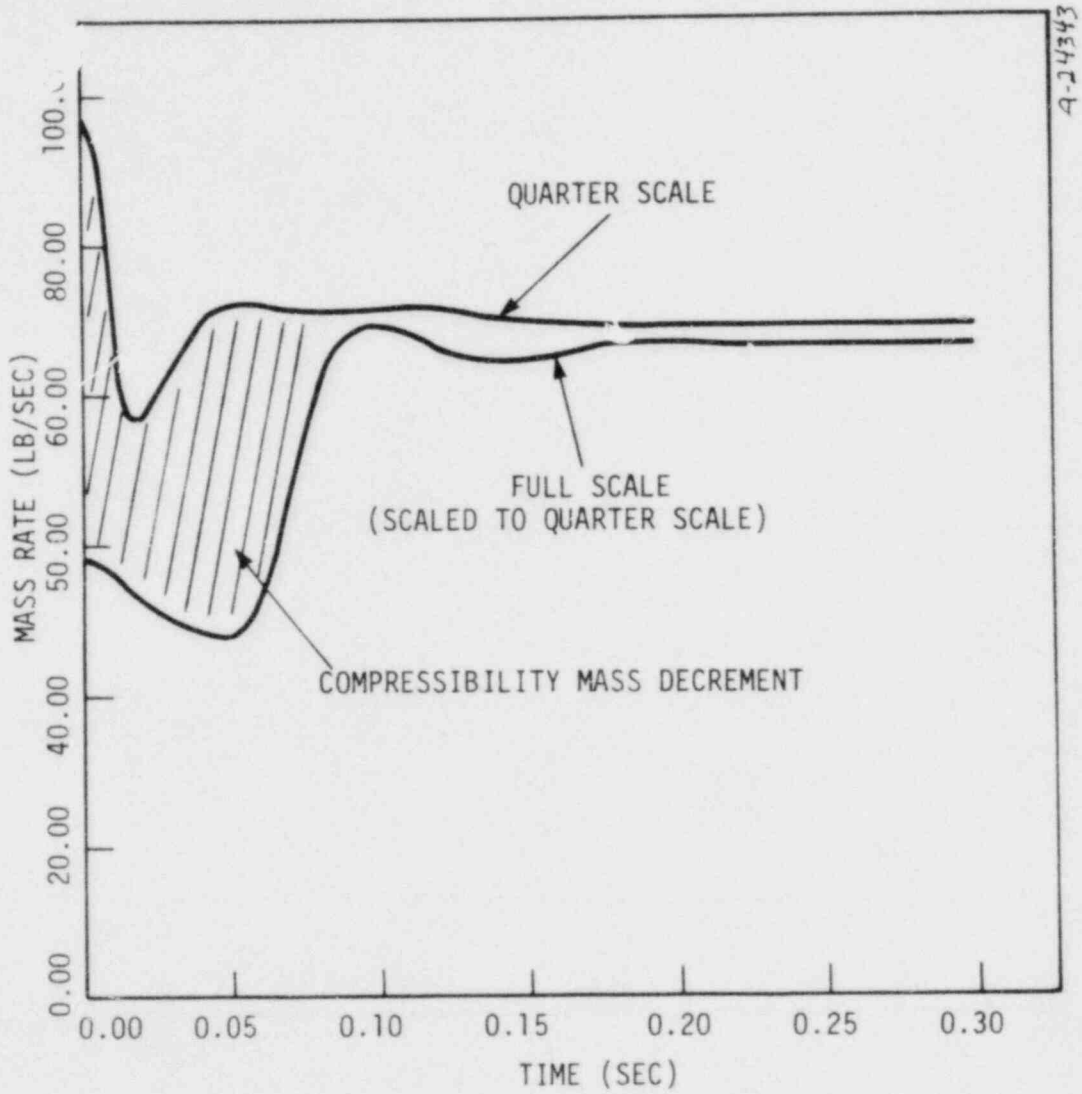
Figure 6-2.   Compressibility study case A.
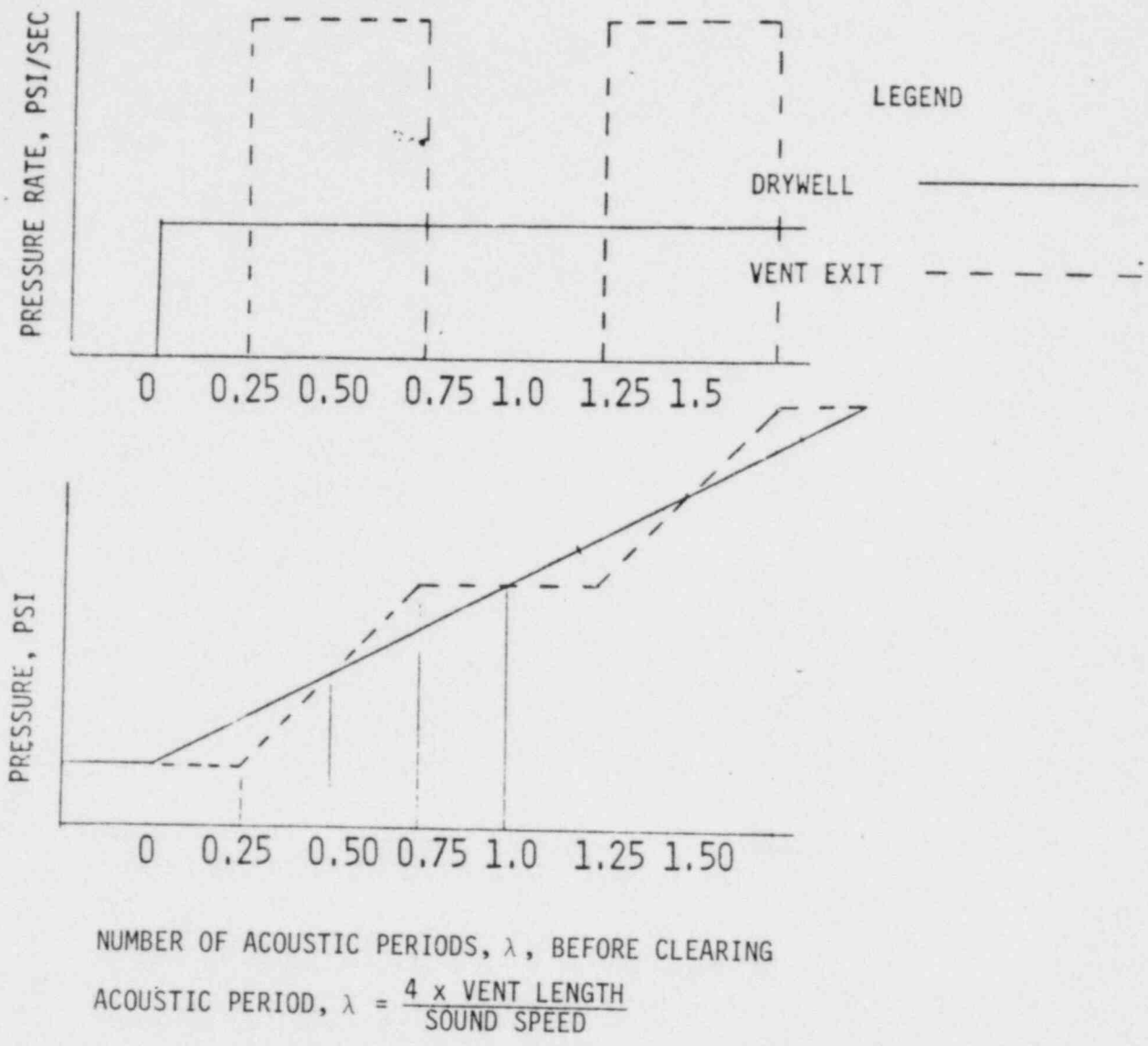
Figure 6-3. Compressibility study case B.
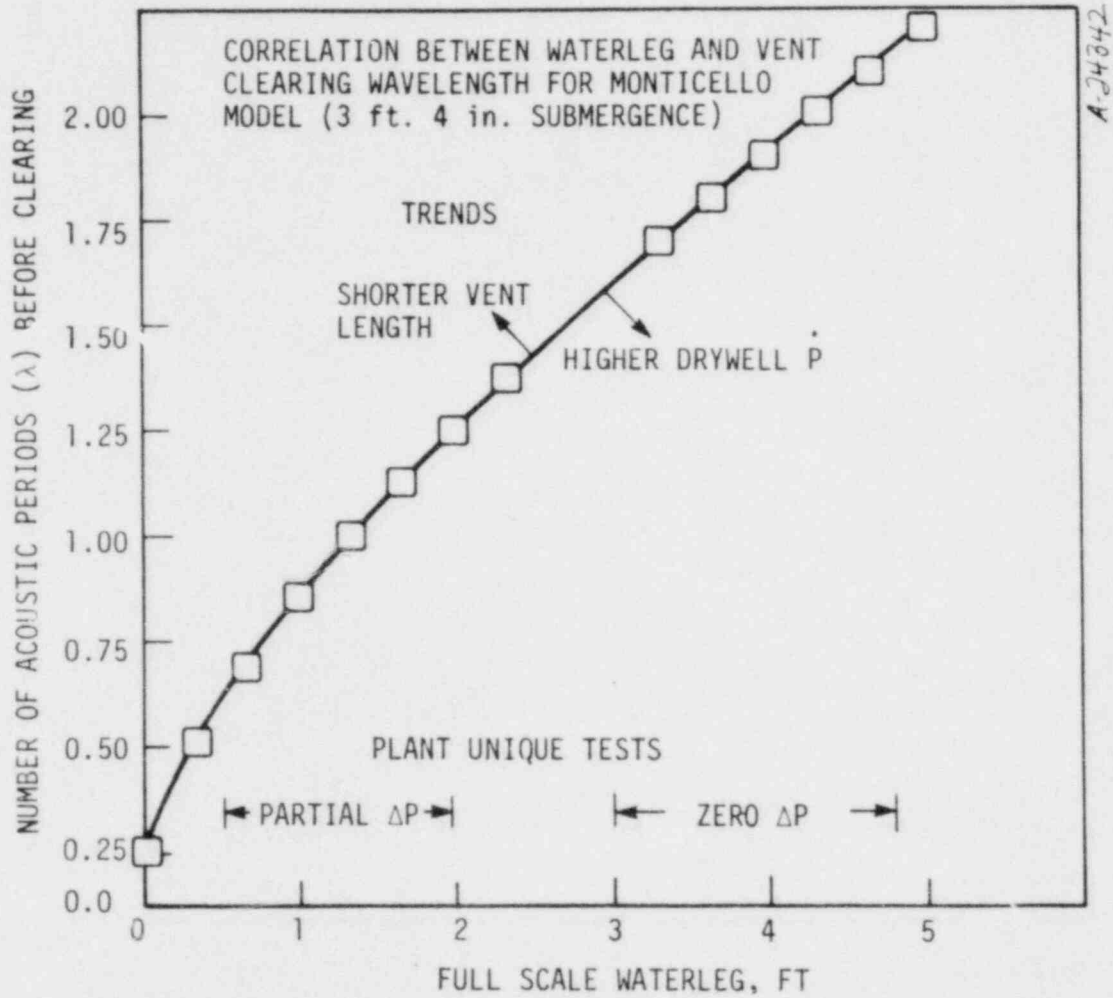
Figure 6-4. Vent pressurization phenomena.

Figure 6-5. Correlation between waterleg and vent clearing time for Monticello model.
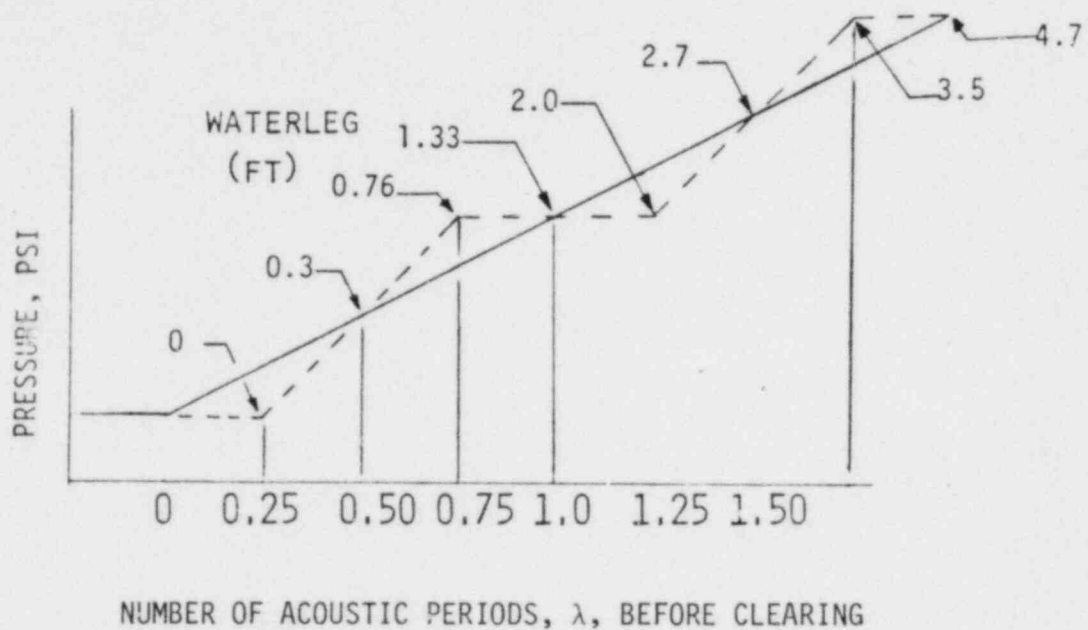
Figure 6-6. Clearing times during pressurization transient.

SECTION 7

ANALYSIS -- MARK ᵢ LOAD SENSITIVITY

Sensitivity of Mark I loads to compressibility effects was evaluated by comparing QSTF loads predicted by the GE/Acurex model to full scale loads predicted by the model. The evaluation included comparisons of predicted peak download, peak upload, and download impulse for various initial conditions.

Differences between predicted full scale loads and predicted QSTF loads were evaluated in two stages: First, effects of known differences between QSTF test conditions and exact prototypical test conditions were quantified; next, effects of compressibility alone, when using quarter scale tests to predict full scale loads, were quantified.

7.1 KNOWN TEST DIFFERENCES

Test condition tolerances for the QSTF Plant-Unique Tests were specified conservatively to ensure that all parameters bounded the idealized or "perfect" QSTF test conditions. Although some of these test tolerance conservatisms are not easily quantifiable, the major test variables (e.g., drywell pressurization rate and vent system resistance) were measured so their degrees of conservatism have been estimated. In addition to test condition tolerances, the vertical vent pipe geometry of the QSTF limited the vent system volume to roughly 60 percent of the scaled volume. Although the drywell and vent system total volume was

correctly scaled (roughly 90 percent of the scaled volume is in the drywell), the smaller volume of the vent system is expected on have a nonconservative effect on the loads. For the Monticello Plant-Unique Tests, three major test tolerance conservatisms and the vent system volume effect are listed below. Although test tolerance values were plant-unique, the Monticello values were typical.

1. Drywell pressurization was 5 percent over the test specification minimum (conservative)

2. Vent system $\frac{fl}{D}$ was 13 percent less than the test specification maximum (conservative)

3. Flow resistance split was 56/44 for the two orifices rather than the baseline 50/50 split (conservative)

4. Vent system volume was 61 percent of the correctly scaled volume (nonconservative)

To quantify the impact of the known test differences on loads, the GE/Acurex model was run in the Monticello QSTF "as tested" configuration and in an idealized or "perfect" quarter scale configuration with drywell $\dot{P}$, vent FL/D, vent volume, and flow resistance split at test specification values. Vent system nodalizations are shown in Figures 5-1 and 7-1. Comparison runs were made at 3 ft. 4 in. submergence (scaled) with ΔP ranging from zero to full. Model results indicate that the known test differences account for conservatisms in the test results of about 4 percent for peak download, 6 percent for peak upload, and 5 percent for peak pool velocity.

7.2   COMPRESSIBILITY EFFECTS

Compressibility effects on pool swell loads were evaluated by
comparing model results for "perfect" quarter scale transients to model
results for the corresponding full scale transients. This isolates
compressible effects from known test difference conservatisms
(Section 7.1). The two vent system nodalizations are shown in Figures 7-1
and 7-2. Comparison runs were made at 3 ft. 4 in. submergence with a
range of waterleg lengths to study the variation of acoustic wave phasing
at clearing and evaluate phasing effects on loads.

Pressure and torus force histories for quarterscale (perfect) and
full scale runs were compared at quarter scale; full scale results were
reduced per Table 3-1. Comparisons which illustrate vent compressibility
effects on pool swell response are presented at three waterleg lengths.

At full ΔP (zero waterleg), the QSTF bubble pressure immediately
rises in response to the drywell pressure ramp (Figure 7-3). As the
volumetric expansion rate of the bubble increases, bubble pressure falls
farther below drywell pressure and eventually peaks. In contrast, at full
scale, compressibility effects delay receipt of the drywell pressure
signal at the exit and then double the bubble pressurization rate. Since
the initial growth rate of the bubble is small, the compressible mass
decrement effect discussed in Section 6 is not strong enough to turn the
pressure around until it has exceeded the QSTF value. Shortly afterward,
the reflected pressure signal from the drywell returns at a zero
pressurization rate (see Figure 6-4) which accelerates the drop in
pressure. Because the full ΔP case clears so early (after one wave travel
time), the zero pressurization signal arrives after peak bubble pressure

(and peak download); compressibility effects cause greater peak download at full scale because the increased bubble pressurization rate dominates the mass decrement effect. Although the download impulse (which is a measure of pool velocity) is roughly the same for QSTF and full scale, the more rapid initial response of the QSTF leads to a greater pool displacement and a greater freespace pressure rise. This, together with the compressibility mass decrement effect, leads to a lower peak upload at full scale as reflected in the smaller maximum differential between bubble and freespace pressure.

Nonconservative effects of compressibility on peak download disappear with a waterleg of only 4 inches, which delays vent clearing to $0.52\,\lambda$ (see Figure 6-5). The greater initial expansion rate of the bubble together with the relatively earlier arrival of the reflected zero pressurization rate signal from the drywell at $0.75\,\lambda$ turn the bubble pressure around fast enough to avoid any download increase due to compressibility. Upload is lower at full scale due to the compressibility mass decrement effect (Figure 7-4).

Although download, upload and impulse continue to be mitigated by compressibility effects with longer waterlegs (less ΔP), the closest approach to a nonconservative download is calculated to occur for clearing at $1.75\,\lambda$. This is in the region where at the time of clearing, the downcomer exit pressure again exceeds the drywell pressure (see Figure 6-4). However, the comparison at zero ΔP (clearing at $1.7\,\lambda$) shows that at full scale, the bubble pressure turns over immediately after clearing, and peak download is less than for quarter scale. This happens because the volumetric growth rate of the bubble at vent clearing rapidly exceeds the ability of the developing exit mass flowrate to maintain the

bubble pressure. In fact, Figure 7-5 shows that just before clearing the waterslug velocity has become large enough so that the double $\dot{P}$ ramp is not being maintained at the vent exit.

The peak values of download, upload and download impulse were plotted from a series of comparative "perfect" QSTF and full scale cases such as those discussed in the previous paragraphs. The peak download comparison (Figure 7-6) shows an 11 percent compressibility increase at full ΔP which essentially disappears for even a 4-inch waterleg. For the range of Mark I plant-unique waterlegs (6 inches or greater), the download is either unaffected or mitigated (by up to 16 percent) by compressibility effects. Similar comparisons at 4 ft. 3 in. submergence showed that the region of nonconservative download was even smaller. A smaller waterleg is required at deeper submergence to delay the peak download past 0.75λ where the reflected zero pressure rate signal helps turn the bubble pressure around.

As discussed in Section 6, the compressibility mass decrement effect introduces a significant conservatism into the full scale upload. The "perfect" QSTF uploads are conservative (Figure 7-7) by from 13 percent to 18 percent. Although the pre-clearing vent acoustic signals appear to reduce the upload conservatism near zero ΔP, the variation in load ratio is much less pronounced than in the download.

The download impulse comparisons shown in Figure 7-8 also indicate nearly uniform mitigation (typically 9 percent) due to compressibility except for an impulse ratio of 1.0 at full ΔP. As discussed in Section 6, download impulse is a measure of maximum pool velocity. As expected, the impulse ratios lie between the values for download and upload.
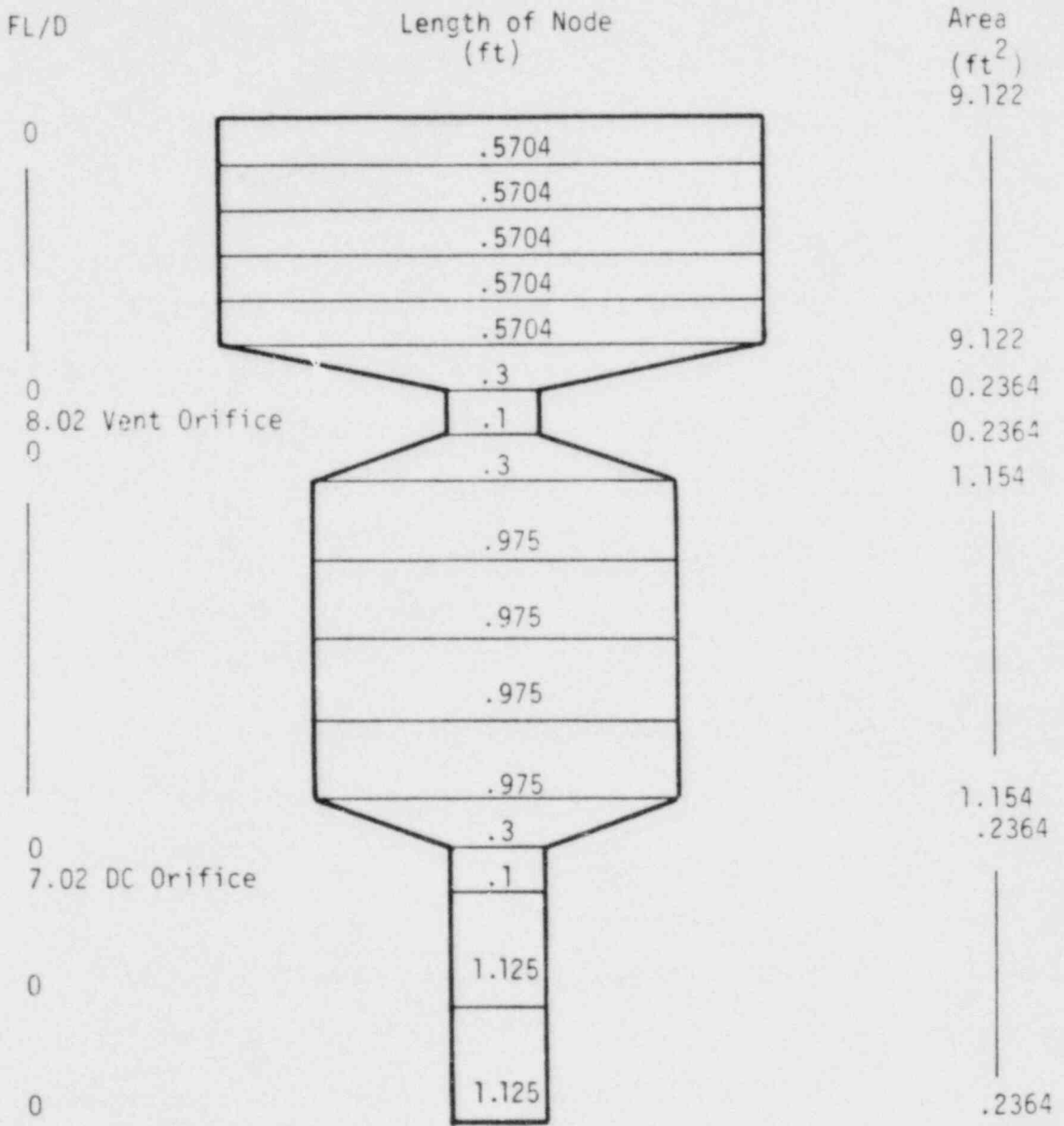
A-24013

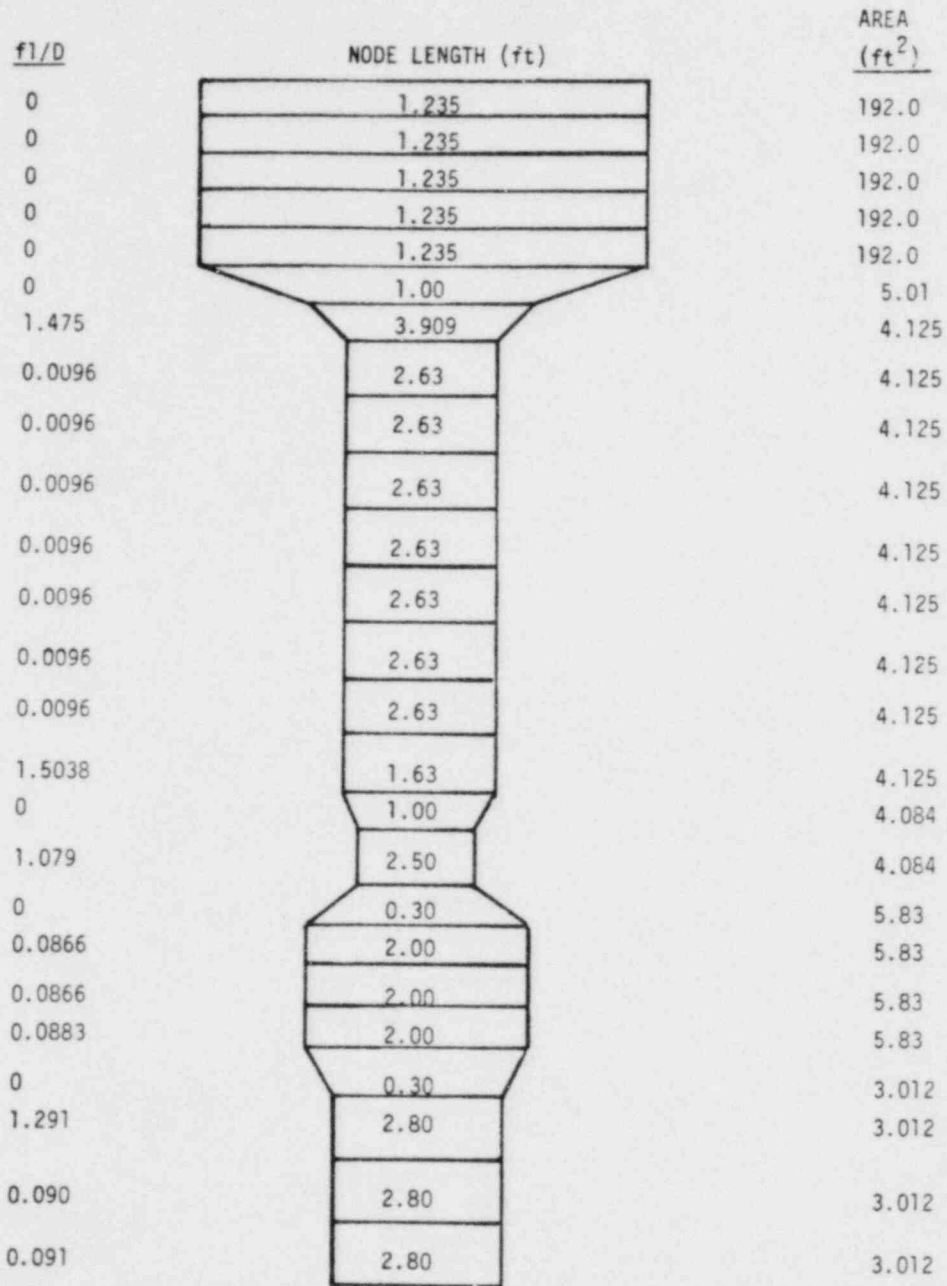
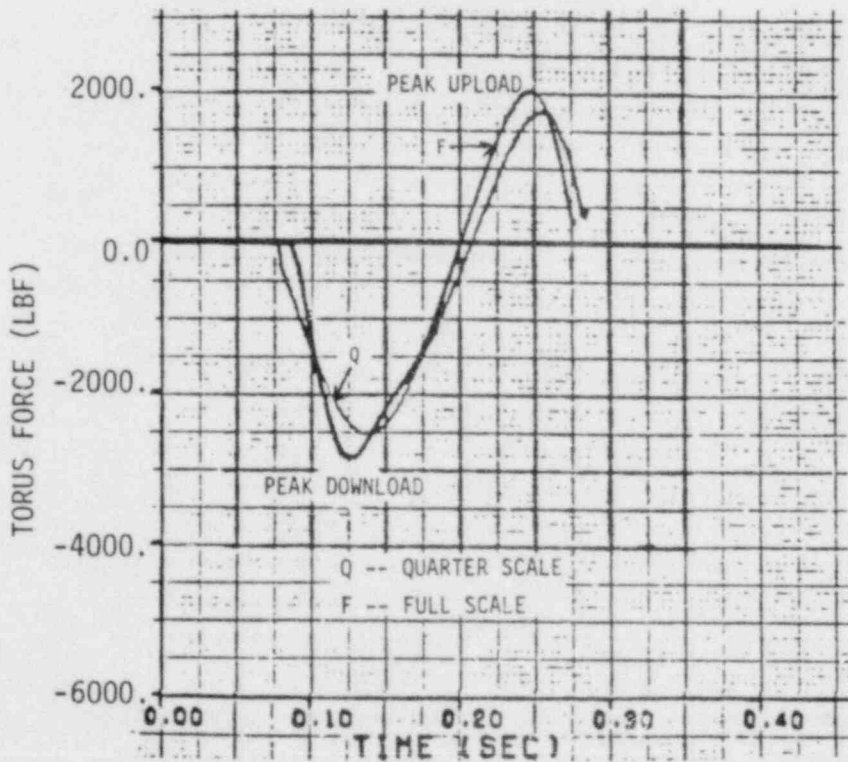Figure 7-1.   Nodal system -- QSTF "Perfect".

fl/D	NODE LENGTH (ft)	AREA (ft^2)
0	1.235	192.0
0	1.235	192.0
0	1.235	192.0
0	1.235	192.0
0	1.235	192.0
0	1.00	5.01
1.475	3.909	4.125
0.0096	2.63	4.125
0.0096	2.63	4.125
0.0096	2.63	4.125
0.0096	2.63	4.125
0.0096	2.63	4.125
0.0096	2.63	4.125
0.0096	2.63	4.125
1.5038	1.63	4.125
0	1.00	4.084
1.079	2.50	4.084
0	0.30	5.83
0.0866	2.00	5.83
0.0866	2.00	5.83
0.0883	2.00	5.83
0	0.30	3.012
1.291	2.80	3.012
0.090	2.80	3.012
0.091	2.80	3.012

Figure 7-2. Nodal system -- full scale.
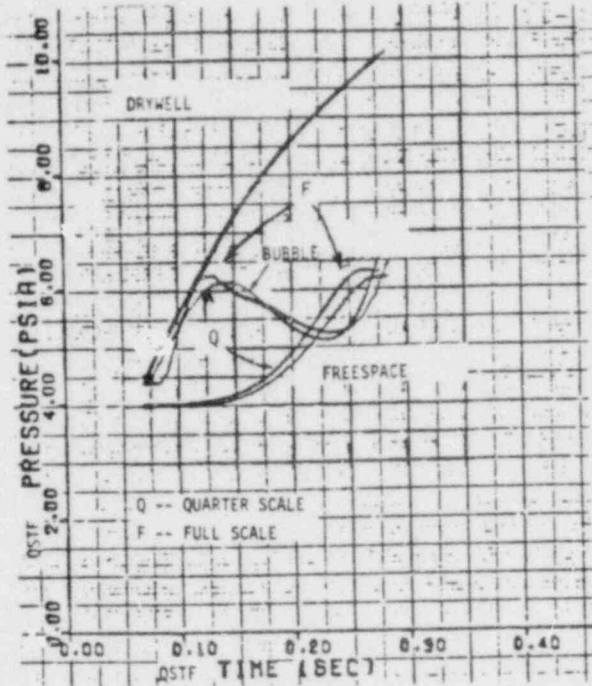
Figure 7-3. Pressure and torus force comparisons for QSTF "perfect" and full scale Monticello model at 3 ft. 4 in. submergence, full ΔP, clears at .25 λ.
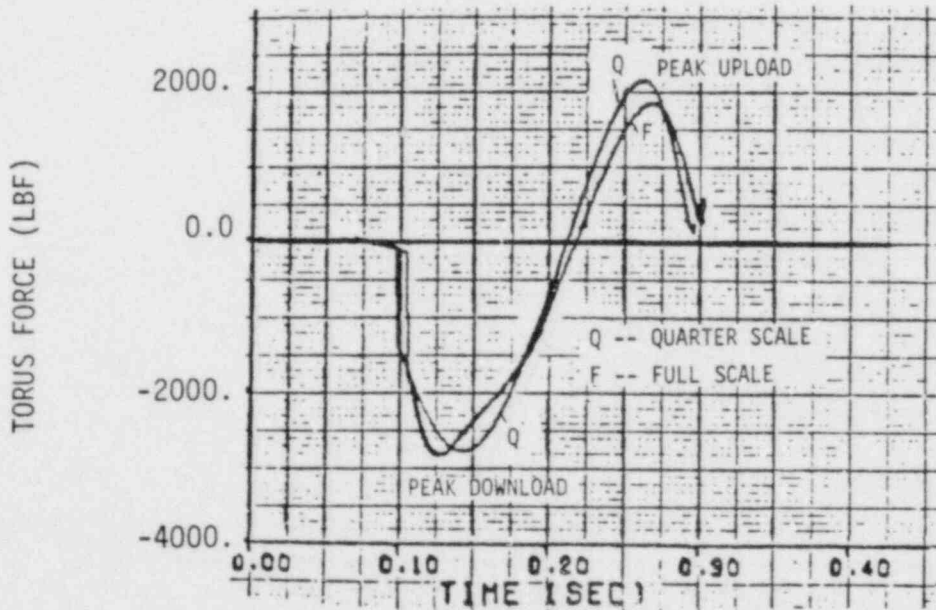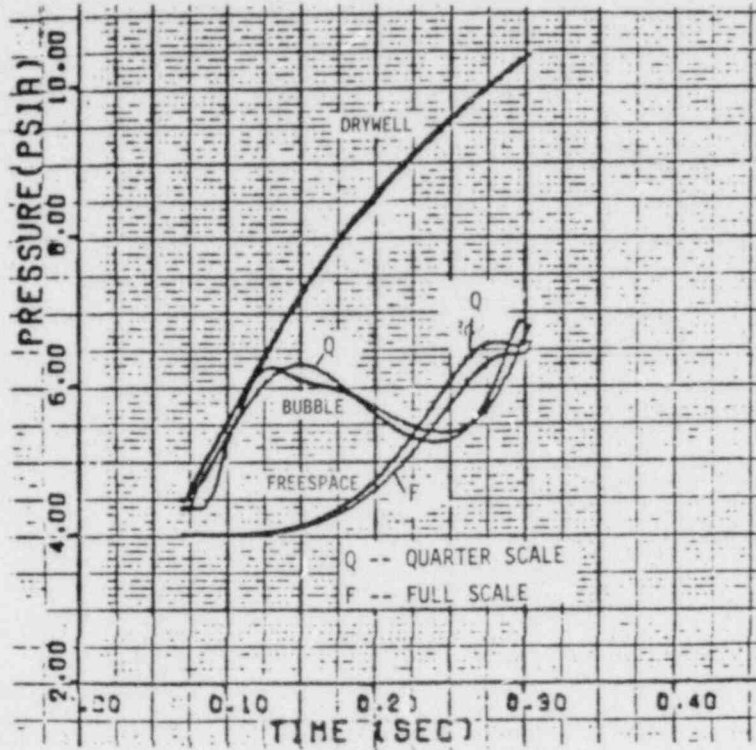
Figure 7-4. Pressure and torus force comparisons for QSTF "perfect" and full scale Monticello model at 3 ft. 4 in. submergence, partial ΔP, clears at .52 λ.
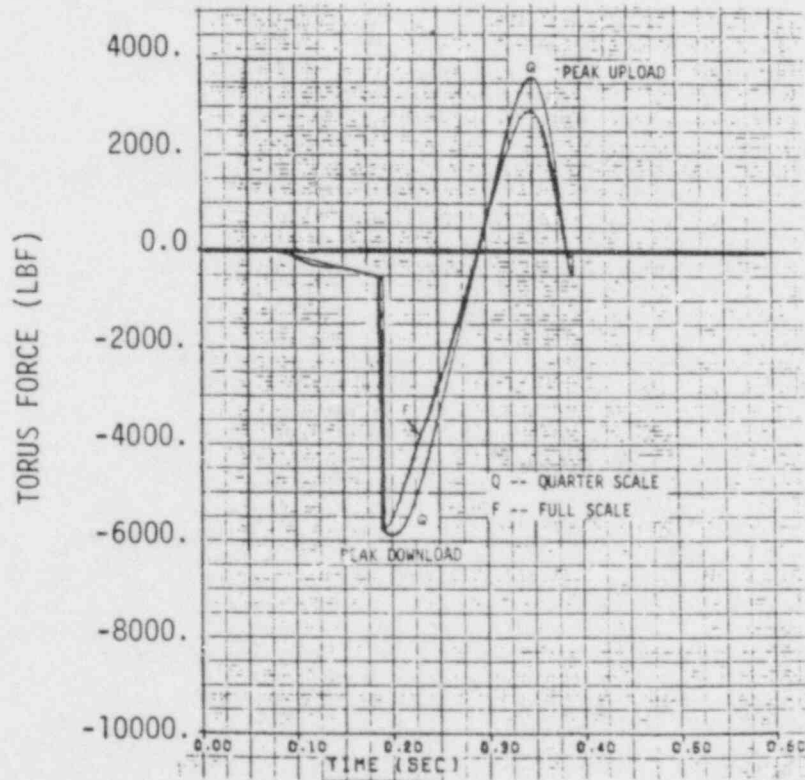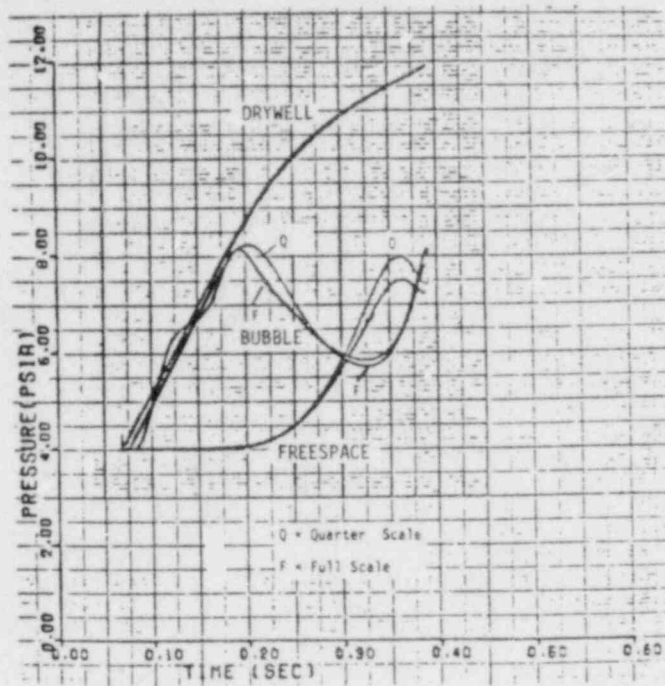
Figure 7-5. Pressure and torus force comparisons for QSTF "perfect" and full scale Monticello model at 3 ft. 4 in. submergence, zero ΔP, clears at 1.7 λ.
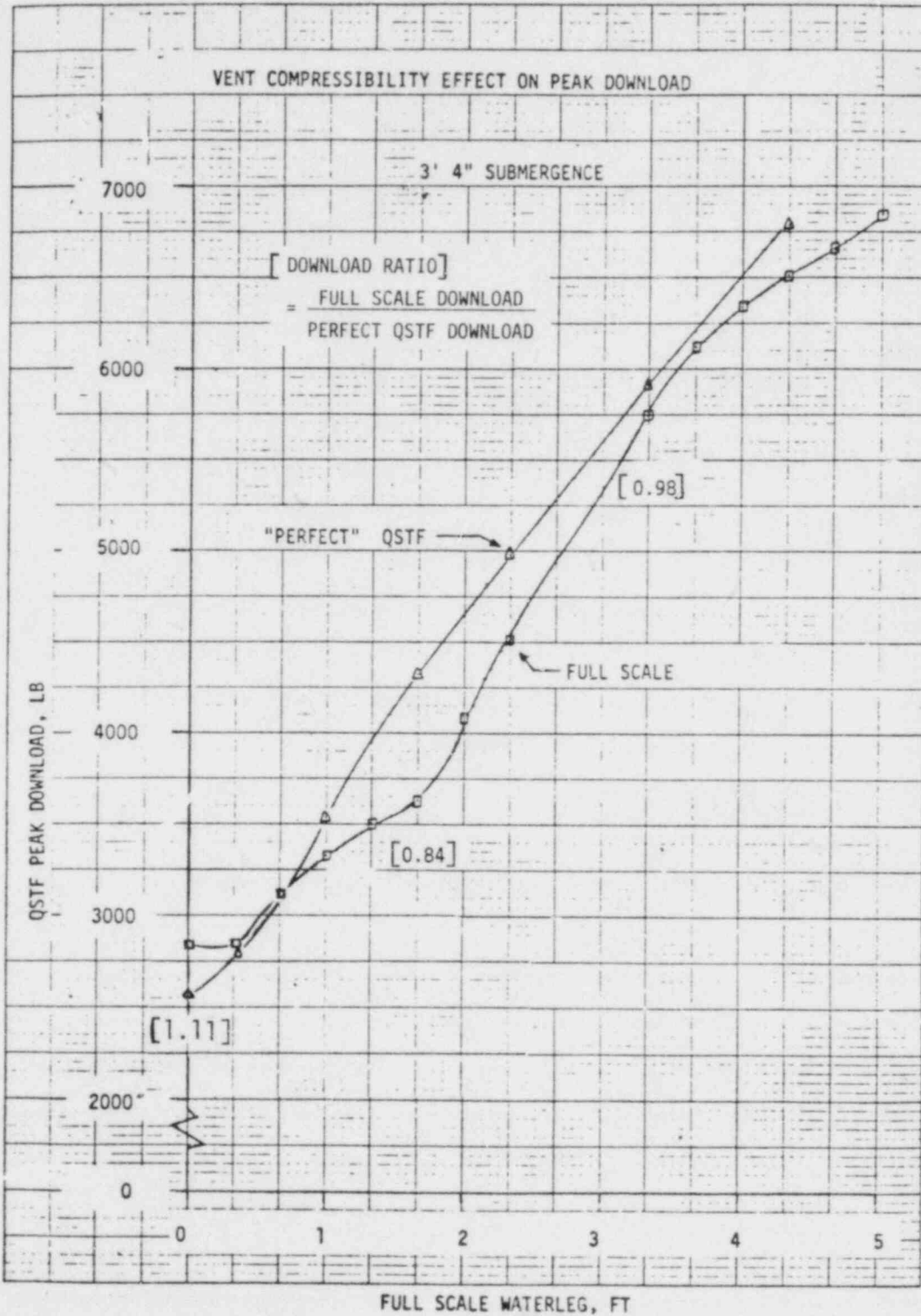
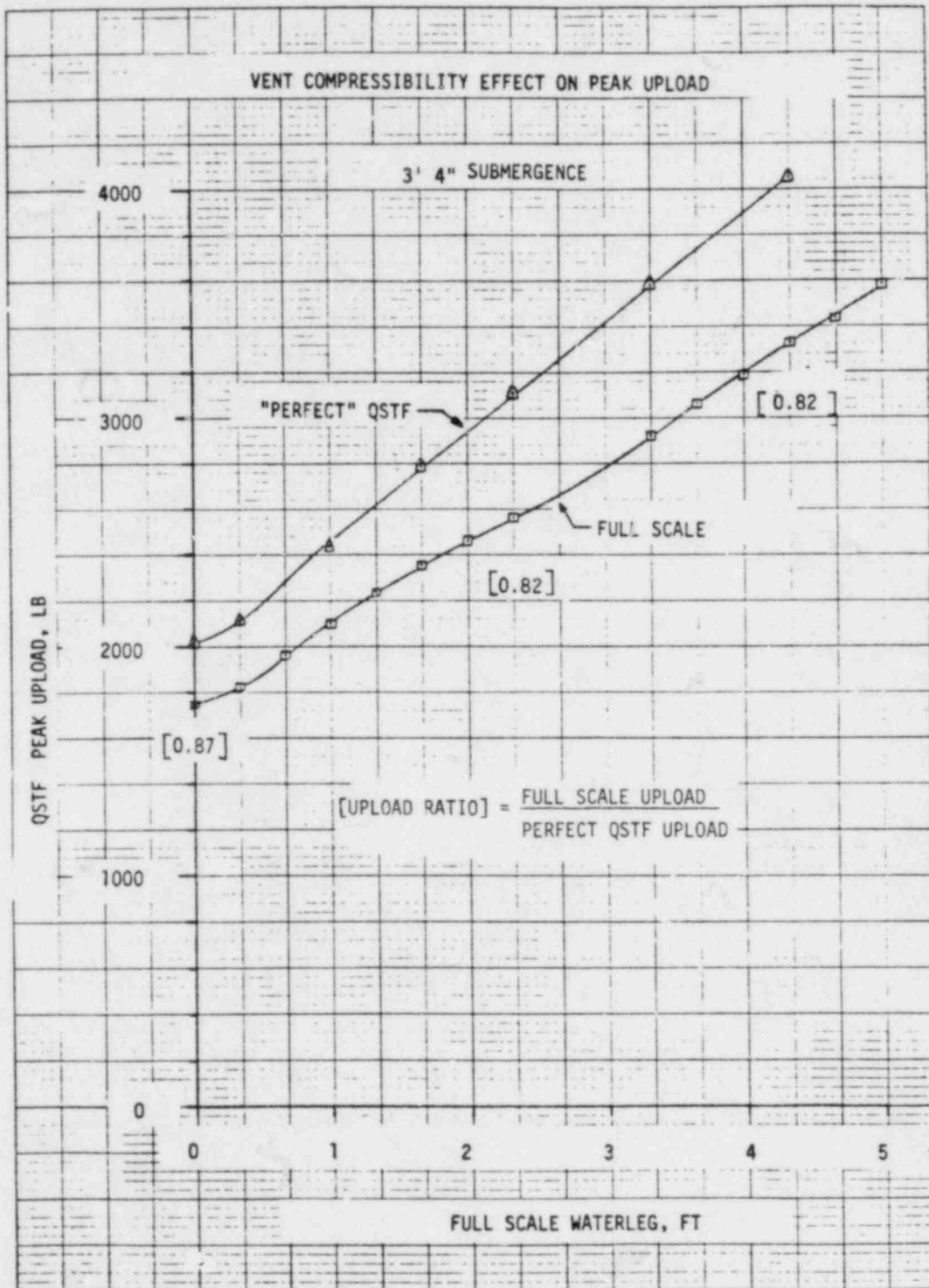Figure 7-6. Vent compressibility effect on peak download.

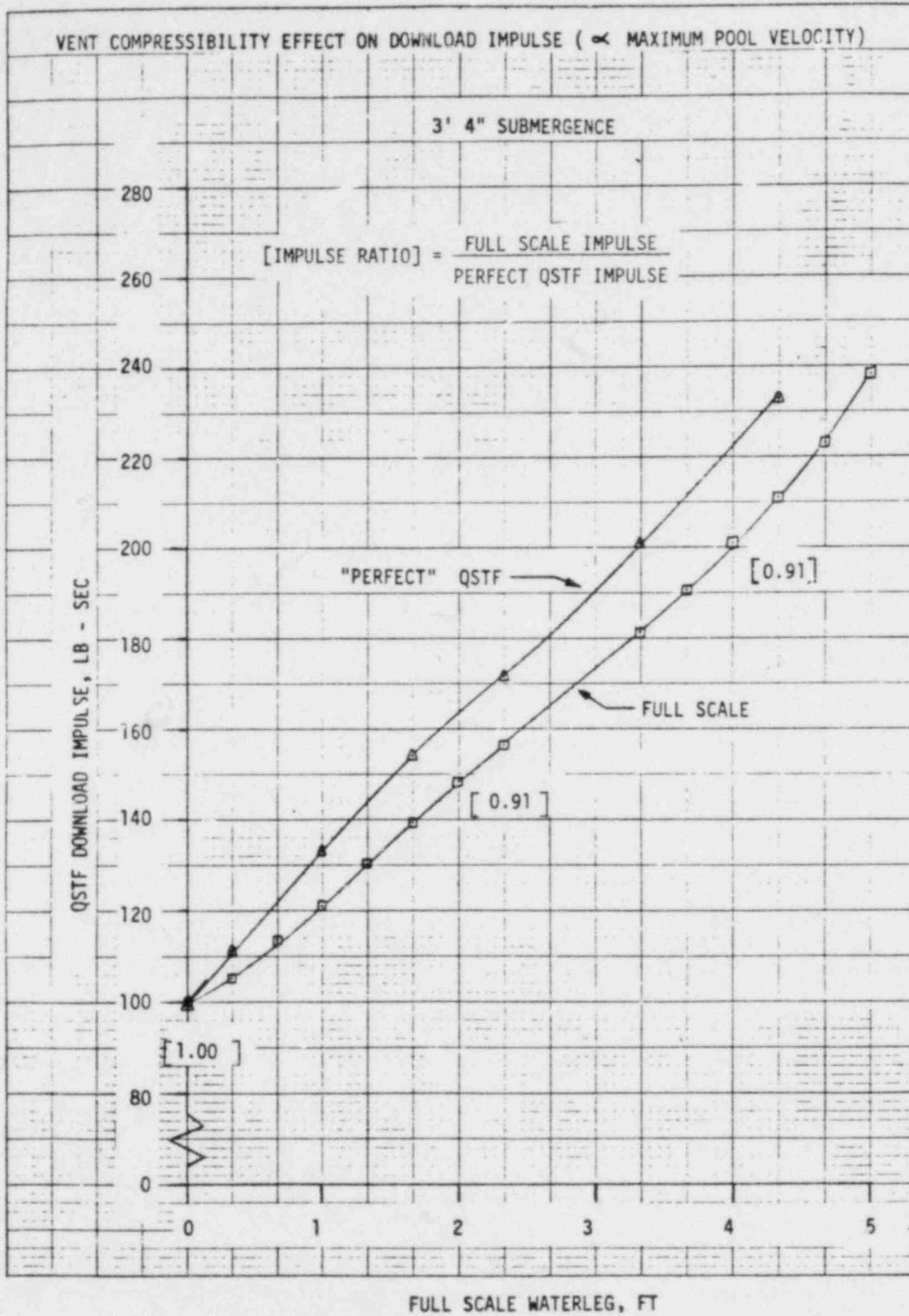Figure 7-7. Vent compressibility effect on peak upload.

Figure 7-8. Vent compressibility effect on download impulse.

SECTION 8

CONCLUSIONS

Conclusions of the vent systems compressibility study are listed below:

1. Pool swell was successfully modeled, including vent system compressibility effects.

2. Known differences between QSTF test conditions and ideal quarter scale conditions introduced 4 to 6 percent conservatism in loads based on QSTF results.

3. Using model analysis and scaling arguments, compressibility effects were identified, explained and quantified.

4. Compressibility effects during pool swell are evident primarily in acoustic delays and in a vent mass flow decrement (relative to incompressible flow).

5. Compressibility effects mitigate the major pool swell loads for existing Mark I operating conditions:

   • Peak download increases by about 11 percent near full ΔP, is unchanged at small waterleg lengths (~4 inches), and decreases by up to 16 percent at moderate ΔP

- Peak upload decreases for all ΔP's, typically by about 15 percent

- Download impulse (or pool swell velocity) is unchanged at full ΔP, decreasing by up to 8 percent at smaller ΔP's.

REFERENCES

1. NEDO-21944, "Mark I Quarter Scale Plant-Unique Tests."

2. "Transient Compressible Manifold Model," unpublished EPRI report.

3. Moody, F. J., "A Systematic Procedure for Scale-Modeling Unsteady Thermo-Fluid Systems," General Electric Co. NEDO-25210.

4. A. A. Sonin and P. W. Huber, "On the Scaling Laws for Air Clearing in Water-Type Pressure Suppression Systems, ASME Journal of Heat Transfer, Vol. 100, No. 4, 1978, pp. 601-604.

5. Anderson, Huber, and Sonin, "Experimental Tests of the Scaling Laws for Air Clearing in Water-Type Pressure Suppression Systems," ASME Journal of Heat Transfer, Vol. 100, No. 4, 1978, pp. 605-612.

6. Galyardt, D. L., "Mark I 1/12-Scale Pressure Suppression Pool Swell Test Program: Phase IV Tests," General Electric Co., NEDO-21492.

7. "Three-Dimensional Pool Swell Modeling of a Mark I Suppression System," EPRI NP-906, Project 693-1, October 1978.

8. Collins and Lai, "Final Air Test Results for the 1/5-Scale Mark I Boiling Water Reactor Pressure Suppression Experiment," UCRL-52371, NUREG/CR-0151, October 1977.

9. NEDO-21888, "Mark I Containment Program Load Definition Report."

10. NEDO-24539, "Mark I Containment Program Full Scale Test Program, Task 5.11," August, 1979.

GENERAL ⊛ ELECTRIC

TECHNICAL INFORMATION EXCHANGE
TITLE PAGE

AUTHOR	SUBJECT	TIE NUMBER	80NED018
	730	DATE May 1980	
TITLE Mark I Containment Program Vent System Compressibility - Effects on Mark I Pool Swell Task 9.1.4.3		GE CLASS I	
		GOVERNMENT CLASS --	
REPRODUCIBLE COPY FILED AT TECHNICAL SUPPORT SERVICES, R&UO, SAN JOSE, CALIFORNIA 95125 (Mail Code 211)		NUMBER OF PAGES 82	

SUMMARY

This report briefly discusses Mark I pool swell
scaling, describes the newly developed vent-flow/
pool-swell model including various test cases, and
presents analytical predictions of the effects of
vent system compressibility on Mark I pool swell loads.

This report was prepared for General Electric
Company by Acurex.

By cutting out this rectangle and folding in half, the above information can be fitted into a standard card file.

DOCUMENT NUMBER _____ NEDO-24778 _____

INFORMATION PREPARED FOR _____ Nuclear Fuel and Services Division

SECTION _____ Training and Technical Services

BUILDING AND ROOM NUMBER _____ 1887-2007 _____ MAIL CODE _____ 886

NED-914 (6/77)